Geophys. J. Int. (2006) **167,** 397–420 doi: 10.1111/j.1365-246X.2006.03018.x

Post-seismic relaxation following the great 2004 Sumatra-Andaman earthquake on a compressible self-gravitating Earth

Fred F. Pollitz,[1] Roland Bürgmann[2] and Paramesh Banerjee[3]

[1] *USGS, Menlo Park, CA,* 94025, *USA. E-mail: fpollitz@usgs.gov*
[2] *Department of Earth and Planetary Sciences, UC Berkley, Berkley, CA 94720, USA*
[3] *Wadia Institute of Himalayan Geology, Dehra Dun, 248001, India*

Accepted 2006 March 20. Received 2006 March 17; in original form 2005 September 2

SUMMARY

The $M_w \gtrsim 9.0$ 2004 December 26 Sumatra-Andaman and $M_w = 8.7$ 2005 March 28 Nias earthquakes, which collectively ruptured approximately 1800 km of the Andaman and Sunda subduction zones, are expected to be followed by vigorous viscoelastic relaxation involving both the upper and lower mantle. Because of these large spatial dimensions it is desirable to fully account for gravitational coupling effects in the relaxation process. We present a stable method of computing relaxation of a spherically-stratified, compressible and self-gravitating viscoelastic Earth following an impulsive moment release event. The solution is cast in terms of a spherical harmonic expansion of viscoelastic normal modes. For simple layered viscoelastic models, which include a low-viscosity oceanic asthenosphere, we predict substantial post-seismic effects over a region several 100s of km wide surrounding the eastern Indian Ocean. We compare observed GPS time-series from ten regional sites (mostly in Thailand and Indonesia), beginning in 2004 December, with synthetic time-series that include the coseismic and post-seismic effects of the 2004 December 26 and 2005 March 28 earthquakes. A viscosity structure involving a biviscous (Burgers body) rheology in the asthenosphere explains the pattern and amplitude of post-seismic offsets remarkably well.

Key words: asthenosphere, normal modes, viscoelasticity.

1 INTRODUCTION

The great 2004 December 26 Sumatra-Andaman earthquake (Fig. 1) ruptured about 1300 km of the Sunda and Andaman subduction zones with combined dip-slip and right-lateral strike-slip motion averaging about 10 m (Stein & Okal 2005; Ammon *et al.* 2005; Banerjee *et al.* 2005). Its magnitude is estimated at $M_w = 9.3$ (Stein & Okal 2005) or $M_w = 9.1$ to 9.2 (Ammon *et al.* 2005; Banerjee *et al.* 2005) depending on the dip of the coseismic fault surfaces thought to have accommodated significant slip. Three months later the $M_w = 8.7$ March 28 Nias earthquake occurred just to the south of the 2004 December rupture. These earthquakes generated large coseismic stress changes in the surrounding volume of the Earth of dimensions ∼1000 km both laterally and vertically. Those regions below the elastic lithosphere cannot sustain these shear stresses and must relax. Because of the size and dimensions of this earthquake, not only the upper mantle but also the lower mantle are expected to flow in response to the earthquake. In order to predict post-seismic relaxation over such large spatial scales and a wide range of temporal scales, it is necessary to account for relaxation of shear stress, including the effects of compressibility and self-gravitation.

Relaxation in shear stress coupled with the perturbations associated with compressibility and self-gravitation has been well investigated for the problem of post-glacial rebound (e.g. Wu & Peltier 1982; Wolf 1991; Han & Wahr 1995; Vermeersen *et al.* 1996). In the framework of viscoelastic normal modes, the construction of Love numbers for the case of surface loads represents the complete solution in the post-glacial case. The solution for post-earthquake relaxation is closely related since it involves simply a different set of boundary conditions to describe the source. Yet applications of post-seismic relaxation analysis have not addressed the entire problem. Restricting attention to a spherical geometry, Pollitz (1992) presented the viscoelastic normal mode solution for the case of earthquake excitation in the absence of gravitation. Piersanti *et al.* (1995) presented a solution to the post-earthquake problem for an incompressible, self-gravitating Earth. Pollitz (1997) presented a solution for the case of a compressible, self-gravitating Earth under the approximation that coupling of body stress perturbations with perturbations in the Earth's gravitational potential could be neglected. This approximation is sometimes referred to as Cowling's approximation in the seismological literature (e.g. Dahlen & Tromp 1998). It is equivalent to explicitly including terms proportional to the Earth's gravitational acceleration g, but neglecting terms proportional to the gravitational constant G when evaluating the set of coupled differential equations for the displacement-stress vector in the normal mode approach (e.g. Wu & Peltier 1982).

© 2006 The Authors
Journal compilation © 2006 RAS

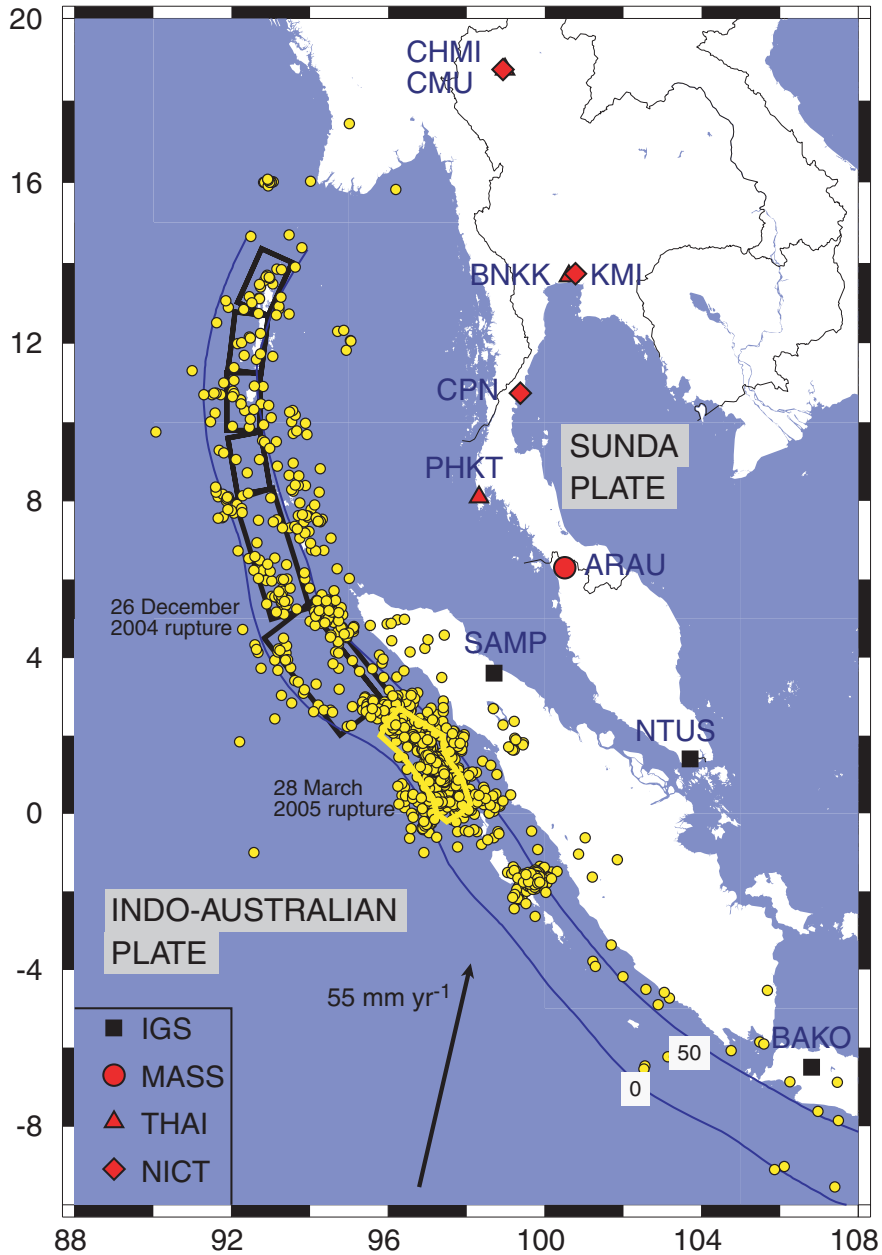

Figure 1. Rupture areas associated with known megathrust earthquakes along the Sumatra-Sunda trench. Black planes are the coseismic rupture of the 2004 December 26 earthquake from Model C of Banerjee *et al.* (2006). Indicated are the 0 and 50 km slab depth contours of Gudmundsson & Sambridge (1998). Epicentres of M $\geq$ 4.0 earthquakes from 2005 March 29 to 2005 August 1 from the NEIC catalogue are superimposed. Selected GPS sites from four regional networks are indicated.

Using a scaling analysis Pollitz (1997) found that on a typical viscoelastic earth model this approximation is adequate for wavelengths less than about 400 km. At greater wavelength it is necessary to include coupling with changes in the Earth's gravitational potential.

Here we construct a viscoelastic normal mode solution for post-earthquake relaxation on a spherically symmetric, compressible, self-gravitating earth model. The equations of quasi-static equilibrium and a stable method of integrating them to obtain the viscoelastic normal modes are presented in Appendices A and B, respectively. We investigate the viscoelastic normal modes associated with two basic models of the viscoelastic asthenosphere, one using a Maxwell rheology and the other a Burgers body rheology. We apply these solutions to the Sumatra-Andaman and Nias earthquake sources in order to investigate the patterns of global post-seismic relaxation to be expected from this earthquake. We shall employ models of earth structure that accurately specify density as a function of depth but which use only a few layers to describe the variation of shear modulus and viscosity with depth. This is done in order to avoid the 'continuous spectrum' of viscous relaxation times that would characterize an earth model with smooth variations of shear modulus and viscosity with depth (e.g. Fang & Hager 1995).

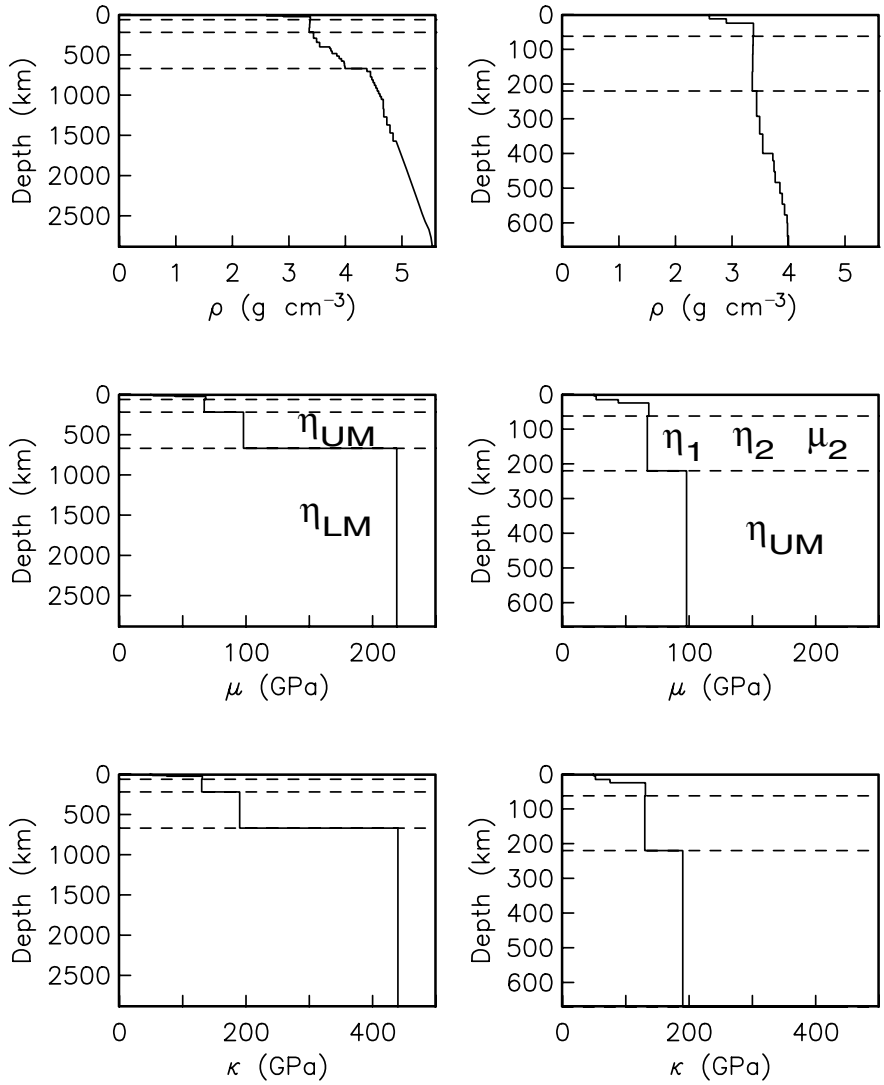

Figure 2. Elastic structure assumed in this study. Discontinuities are present at depth 220, 670, and 2891 km. The steady state and transient viscosity and transient shear modulus in the asthenosphere are η_1, η_2, and μ_2, respectively. The upper mantle and lower mantle viscosity are η_{UM} and η_{LM}, respectively.

2 VISCOELASTIC NORMAL MODES OF ASTHENOSPHERE RELAXATION MODELS

2.1 Viscoelastic model structure

The elastic stratification of the models considered here is shown in Fig. 2. It has the density structure of PREM (Dziewonski & Anderson 1981), which possesses major discontinuities at depth 220 km (bottom of asthenosphere), 670 km (upper mantle–lower mantle boundary) and 2891 km (core–mantle boundary). We introduce an additional discontinuity at 62 km depth which is meant to represent the top of the oceanic asthenosphere. This is the approximate depth to sharp boundary marking a low-velocity zone in the mid-Pacific (Gaherty *et al.* 1996). In the spherical volumes between these discontinuities we prescribe constant shear modulus and bulk modulus using average values of these parameters from PREM. In viscoelastic models we further prescribe constant viscosity values between these discontinuities. This is done in order to avoid the continuous spectrum of relaxation times that results from a continuous distribution of shear modulus or viscosity with depth (Fang & Hager 1995).

Viscoelastic models are defined with a Burgers body rheology (e.g. Yuen & Peltier 1982) in the asthenosphere and Maxwell rheology in the remaining upper and lower mantle. The viscosity structure is parametrized with η_1 and η_2 between 62 km and 220 km depth, η_{UM} between 220 km and 670 km depth, and η_{LM} between 670 km and 2891 km depth (Fig. 2). These are the steady state and transient viscosity in the asthenosphere, the upper mantle viscosity, and lower mantle viscosity, respectively. Two other parameters to describe the Burgers body rheology are the steady state shear modulus μ_1, which is just the elastic shear modulus, and the transient shear modulus μ_2. The Burgers body rheology in the asthenosphere reduces to a Maxwell rheology if $\eta_2 = \infty$. Following Pollitz (2003a) we assume $\mu_2 = \mu_1$. We consider two viscosity structures:

Rheology 1: $\eta_1 = 5 \times 10^{17}$ Pa s, $\eta_2 = \infty$, $\eta_{UM} = 10^{20}$ Pa s, $\eta_{LM} = 10^{21}$ Pa s.

Rheology 2: $\eta_1 = 10^{19}$ Pa s, $\eta_2 = 5 \times 10^{17}$ Pa s, $\eta_{UM} = 10^{20}$ Pa s, $\eta_{LM} = 10^{21}$ Pa s.

© 2006 The Authors, *GJI*, **167,** 397–420
Journal compilation © 2006 RAS

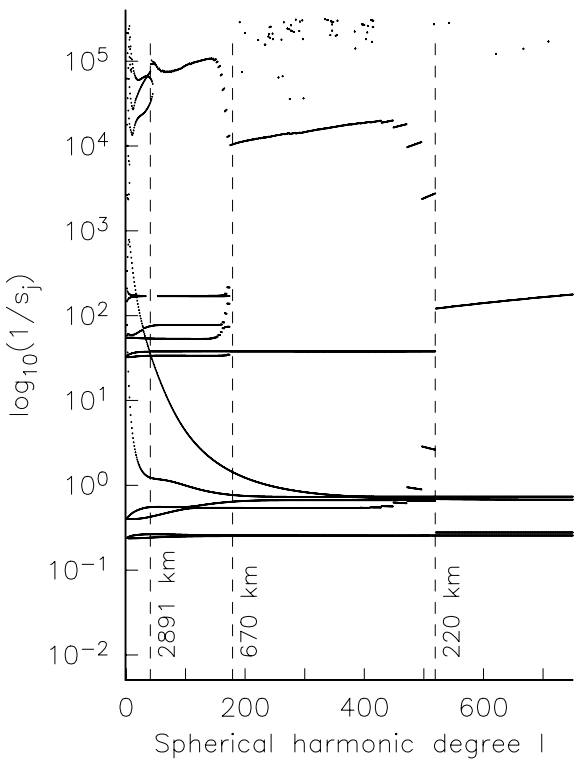

Figure 3. Relaxation time of viscoelastic normal modes on rheology 1 as a function of spherical harmonic degree. There are altogether 6672 modes identified with relaxation times less than 3.189×10^5 yr. Dashed lines indicate the *l*-value associated with a depth of three wavelengths equal to the given depth. This is where the given depth is used as the radius of an inviscid sphere where the radial integration is begun. Because of the discrete layering of the Earth model, the true *l*-value associated with a given starting depth is slightly larger than that indicated on the figure.

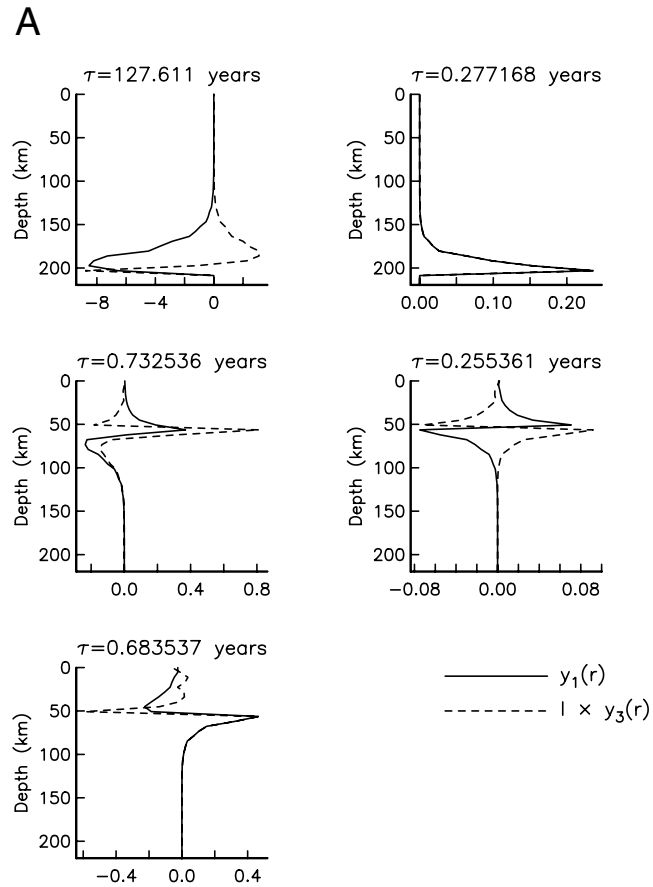

Figure 4. Mode eigenfunctions $y_1(r, s_j)$ and $l \times y_3(r, s_j)$ normalized by $\sqrt{\epsilon_j s_j}$ on rheology 1. (a) Stable relaxation modes of $l = 545$ for $1/s_j < 3.189 \times 10^5$ yr. (b) Stable relaxation modes of $l = 545$ for a few modes with $1/s_j > 3.189 \times 10^5$ yr. (c) Unstable (RT) relaxation modes of $l = 545$ for the five fastest growing modes.

Each viscosity structure has a low viscosity value of 5×10^{17} Pa s in the asthenosphere based on Pollitz *et al.* (1998). In rheology 1 it is the steady state viscosity, and in rheology 2 it is the transient viscosity.

2.2 Response with Maxwell rheology

Fig. 3 presents a dispersion diagram of relaxation times as a function of spherical harmonic degree for rheology 1. The complicated appearance of this diagram arises from several factors:

(1) the use of three distinct viscoelastic layers and an elastic lithosphere,
(2) the presence of an inviscid fluid core,
(3) the presence of a continuously varying density profile (in practice, represented with more than 100 layers),
(4) compressibility effects and
(5) a degree-dependent position of the 'core–mantle' boundary.

The last factor refers to the practical implementation of the integration of eqs (A13) and (A22) in which we start the radial integration at a depth of three wavelengths, where one wavelength equals

$$\frac{2\pi a}{l + \frac{1}{2}}$$

If this depth is greater than the actual depth of the core mantle boundary, then starting conditions (A15) and (A24) are specified at $r = b$, otherwise they are specified at a depth of three wavelengths. This starting depth is rounded off to the top or bottom of the nearest layer, hence the staggered appearance of a few dispersion branches as *l* increases through certain ranges. The starting radius of integration is $r = b$, that is, a depth of 2891 km, for $l \leq 40$ and shallows to a depth of 160 km for $l = 750$ This is accurate for seismic sources in the lithosphere and evaluation of deformation in the lithosphere, avoiding the need to consider deep relaxation effects for shorter wavelengths.

The vertical and horizontal mode eigenfunctions are shown in Fig. 4(a) for $l = 545$ on rheology 1 and $\tau = 1/s_j < 3.169 \times 10^5$ yr. As defined in eq. (A26), positive s_j represent an exponentially-decaying mode associated with a pole $s = -s_j$ in the Laplace transform domain. The dominant mode in the lithosphere is that with relaxation time 0.683537 yr. Other modes are either of smaller amplitude in the lithosphere and/or confined to the region near the boundary at 220 km, which is at a depth of three wavelengths and thus represents the depth to the top of a spherical shell below which an inviscid sphere is specified as a boundary condition. Fig. 5 shows the eigenfunctions for $l = 180$ on rheology 1 and $\tau = 1/s_j < 3.169 \times 10^5$ yr. The depth to the inviscid sphere in this case is 670 km. The dominant mode is that with relaxation time 1.41856 yr. Its eigenfunction values in the lithosphere are 10 times larger than that of any other mode. This shows that even at fairly long wavelength, that is, 223 km in this case, the relaxation response in the lithosphere is

© 2006 The Authors, *GJI*, **167,** 397–420
Journal compilation © 2006 RAS

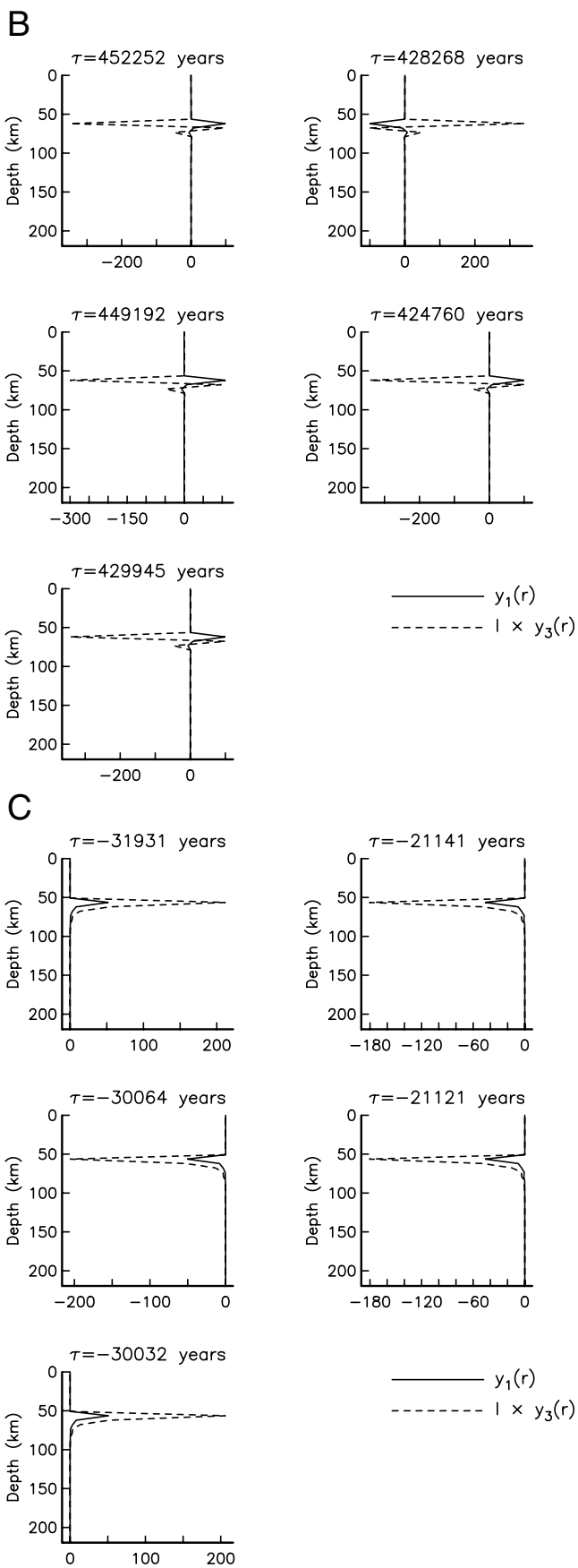

Figure 4. (*Continued.*)

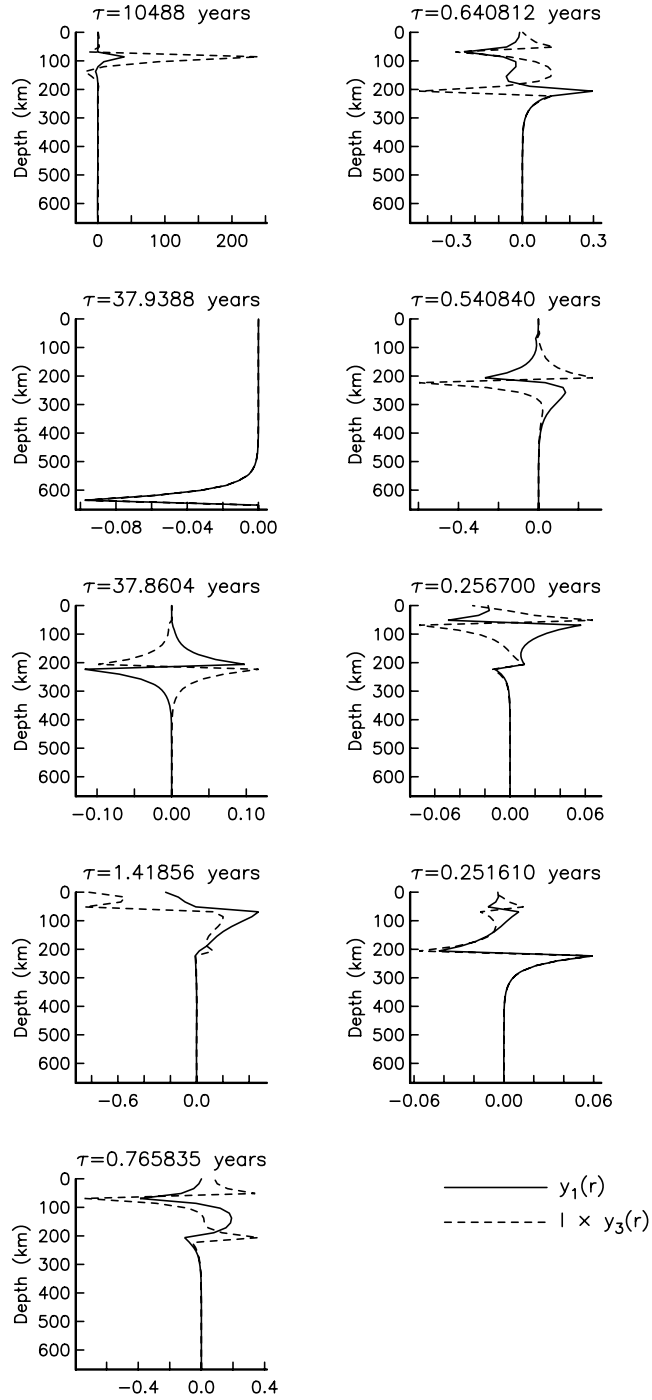

Figure 5. Mode eigenfunctions $y_1(r, s_j)$ and $l \times y_3(r, s_j)$ normalized by $\sqrt{\epsilon_j s_j}$ on rheology 1. Stable relaxation modes of $l = 180$ for $1/s_j < 3.189 \times 10^5$ yr.

sensitive primarily to relaxation in the low-viscosity asthenosphere rather than the higher-viscosity upper mantle below 220 km.

In Fig. 3 we excluded from the dispersion set those modes corresponding to $\tau \geq 3.169 \times 10^5$ yr. That is because at fixed l, we find a very large number of modes associated with these longer relaxation times. These are presumably a mixture of compressible modes and buoyancy modes, of which there are expected to be theoretically infinitely many (Han & Wahr 1995) because of the use of a compressible rheology and the presence of a continuously

© 2006 The Authors, *GJI*, **167,** 397–420
Journal compilation © 2006 RAS

varying density profile. Five such modes are shown in Fig. 4(b). All of them have peak energy at depths just below the base of the lithosphere. They are, in fact, similar to the unstable RT modes discussed by Plag & Jüttner (1995), Hanyk *et al.* (1999) and Vermeersen & Mitrovica (2000). The unstable modes are associated with negative s_j, that is, poles of the displacement response on the positive real s-axis, and are termed Rayleigh-Taylor unstable modes by Plag & Jüttner (1995) because they arise fundamentally from the failure of the PREM earth model to satisfy the Adams–Williamson equation. In our model, a substantial departure from the Adams–Williamson equation occurs between 62 and 220 km depth in the relatively low-density asthenosphere. This produces admissible solutions to the equations governing viscoelastic normal modes for negative s_j, that is, modes that grow with time according to eq. (A26). The five fastest-growing unstable modes for $l = 545$ are shown in Fig. 4(c). We find that both the stable modes at large $\tau > \sim 3 \times 10^5$ yr and the unstable modes are associated with surface eigenfunctions of amplitude generally 2 to 5 orders of magnitude smaller the small-τ stable modes. However, a few unstable modes are found with displacement amplitudes of the same order as the dominant stable mode. Plag & Jüttner (1995) hypothesize that other processes (effects of stress-dependent rheology; coupling with thermal stresses) not included in the linear viscoelastic theory should operate in order to neutralize the unstable mode excitation. Vermeersen & Mitrovica (2000) argue that in the event that unstable modes were ever excited in the past, the Earth should have re-adjusted to a stable density and compressibility configuration over geologic time. We adopt this viewpoint and hypothesize that the actual density and compressibility structure should satisfy the Adams–Williamson equation and that the stable modes identified here would closely correspond to the viscoelastic modes of the hypothetical stable structure. With this restriction to the stable modes, we find that calculated post-seismic deformation for the long 2004 Sumatra-Andaman rupture differs only slightly from that calculated using the approximate treatment of Pollitz (1997), for which no unstable modes are admissible.

2.3 Response with Burgers body rheology

Fig. 6 shows the dispersion diagram obtained on rheology 2 for $\tau < 3.189 \times 10^5$ yr. Comparison with Fig. 3 reveals some details of the influence of asthenosphere relaxation on the model responses. The effect of the Burgers body rheology is to increase the total number of stable modes, with several new dispersion branches appearing with τ near the material relaxation time associated with the steady state asthenosphere viscosity—$\eta_1/\mu_1 = 4.7$ yr. The eigenfunctions associated with the ten identified stable modes on rheology 2 for $l = 545$ are shown in Fig. 7. The modes associated with the largest lithosphere amplitudes are those associated with relaxation times 18.4659 and 0.175124 yr. These are clearly associated with upper asthenosphere relaxation governed by relaxation times that are proportional to the steady state and transient viscosities of the asthenosphere, respectively.

As with rheology 1, modes sensitive to primarily asthenosphere relaxation are identified as doublets with nearly identical τ (Fig. 4a). On rheology 1, one of the doublets has τ values of 0.255361 and 0.277168 yr that are close to the material relaxation time of the asthenosphere—0.235490 yr. The other doublet has τ values of 0.683537 and 0.732536 yr. Fig. 4(a) shows that the relaxation pattern in the modes of the first doublet are completely different, whereas they are similar for the second doublet. On rheology 2 there are three sets of doublets, the first with τ values of 0.121358 and 0.126251 yr, the second with τ values of 0.175124 and 0.178232 yr, and the third with τ values of 9.95189 and 10.3831 yr. The modes in first doublet of rheology 2 have very similar mode eigenfunctions with energy concentrated near the base of the asthenosphere and very small energy in the lithosphere (Fig. 7). The second doublet of rheology 2 behaves like the second doublet of rheology 1, with all mode eigenfunctions having energy concentrated near the top of the asthenosphere and relatively large amplitudes in the lithosphere. The third doublet of rheology 2 behaves like the first doublet of Model 1, with one mode sensitive to lower asthenosphere relaxation and the other to upper asthenosphere relaxation.

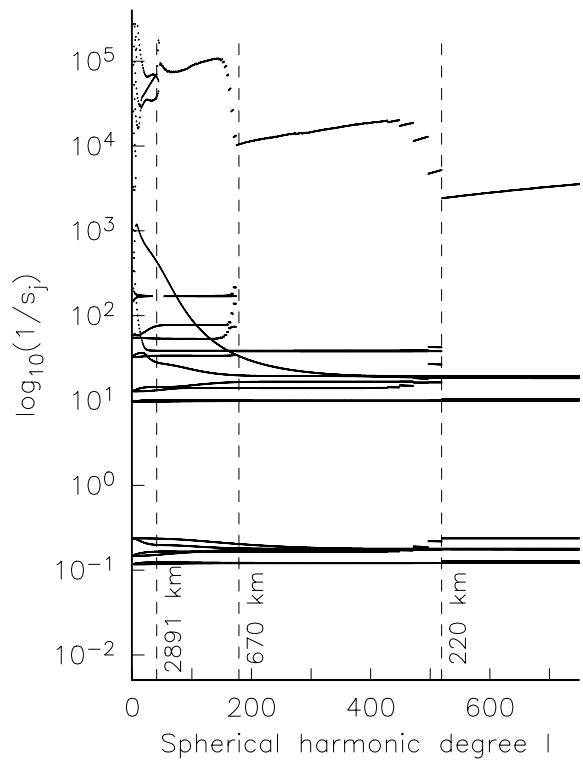

Figure 6. Relaxation time of viscoelastic normal modes on rheology 2 as a function of spherical harmonic degree. There are altogether 10 794 modes identified with relaxation times less than 3.189×10^5 yr. As in Fig. 3 dashed lines indicate the l-value associated with a depth of three wavelengths equal to the given depth.

3 APPLICATION TO THE 2004 SUMATRA-ANDAMAN AND 2005 NIAS EARTHQUAKES

Post-seismic effects from past great megathrust earthquakes are evident even several decades after the event as demonstrated using GPS velocity observations in the regions of the $M_w = 9.5$ 1960 Chile earthquake (Hu *et al.* 2004) and $M_w = 9.2$ 1964 Alaska earthquake (Freymueller *et al.* 2000). These authors attribute most of the signal in the velocity measurements to viscoelastic relaxation of the mantle. The signal is especially large because of the great length and width of such ruptures.

As a first order approach, we use slip models for the $M_2 = 9.2$ 2004 December 26 and $M = 8.7$ 2005 March 28 earthquakes (Fig. 1) constrained by far-field static offsets and seismic waves, respectively. For the 2004 event this carries the advantage of capturing essentially all of the moment release associated with the earthquake

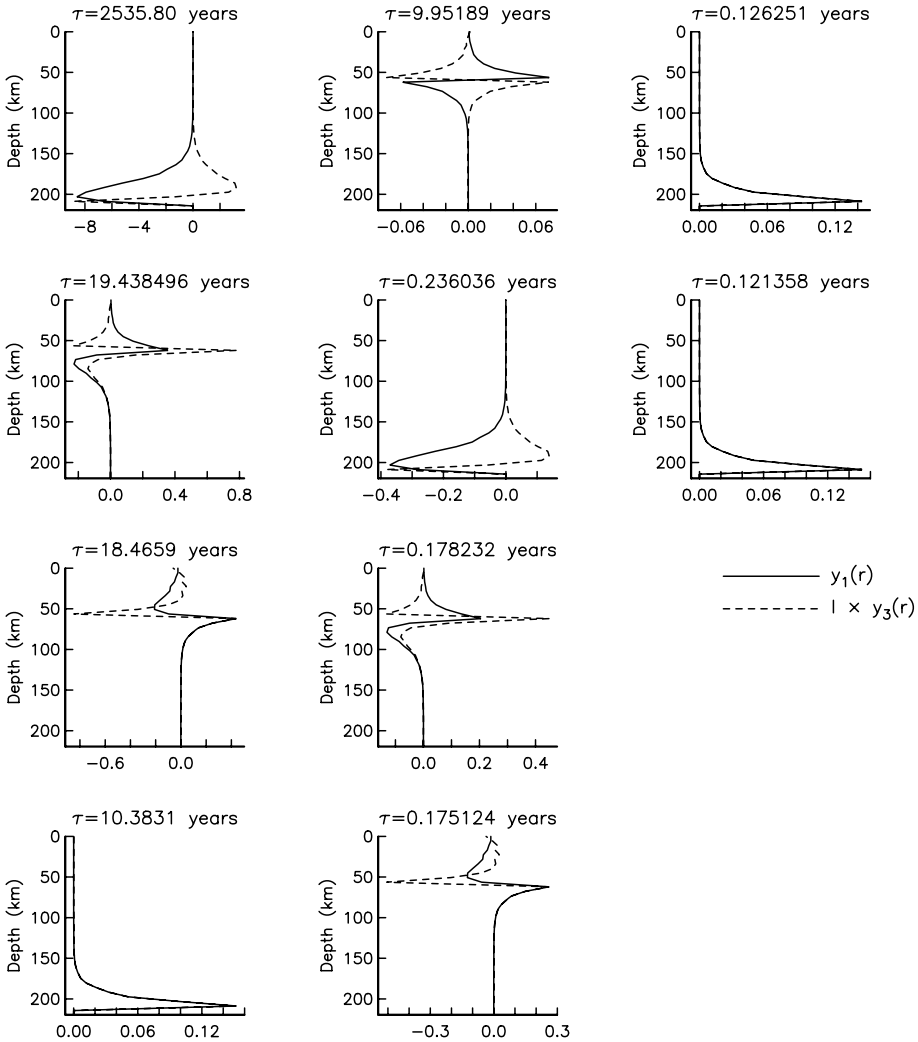

Figure 7. Mode eigenfunctions $y_1(r, s_j)$ and $l \times y_3(r, s_j)$ normalized by $\sqrt{\epsilon_j s_j}$ on rheology 2. Stable relaxation modes of $l = 545$ for $1/s_j < 3.189 \times 10^5$ yr.

sequence, which may have included very slow rupture of the northern half of the rupture based on free oscillations (Stein & Okal 2005); Banerjee *et al.* (2005) argue that much of the slow rupture was not detected even at the longest seismic periods (up to ∼1 hr). For this purpose we use the preferred coseismic slip model of Banerjee *et al.* (2006), which was derived from a set of 142 horizontal GPS displacement vectors and 30 vertical GPS displacement vectors. The models derived in Banerjee *et al.* (2006) are refinements of those derived in Banerjee *et al.* (2005), which were derived with a smaller set of coseismic offsets; the larger data set fills in many gaps in Thailand and Indonesia. An example is shown for Model C of Banerjee *et al.* (2006) in Fig. 8(a). This model demonstrates that coseismic static displacement computed on the PREM model with an average ∼10 m slip on a 1300-km-long, 100–140-km-wide set of faults yields an excellent fit to the observed static offsets. Banerjee *et al.* (2005) found that slip models without the Andaman segment, that is, the northern ∼650 km of the rupture, fit the observations significantly worse than models that include the Andaman segment.

We also use the 2005 March 28 Nias earthquake the source model derived by Banerjee *et al.* (2006) using 32 regional GPS sites. The fit obtained by the simple five-plane model is excellent (Fig. 9). This model, obtained with a dip of 15°, corresponds to magnitude $M_w = 8.66$. This is larger than the magnitude $M_w = 8.5$ obtained by Ji (2005) from seismic wave analysis using the same dip. This suggests a substantial difference between the moment at seismic periods and that determined geodetically, which may imply an additional contribution from afterslip occurring within a short time after the earthquake. Together, the 2004 December and 2005 March slip models provide the source models for calculating coseismic and post-seismic displacements at selected sites, resulting in model time-series for a given rheology model. Similarly to the post-seismic displacements, coseismic displacements are calculated in a layered spherical geometry (Pollitz 1996).

As an example using on the 2004 December source, Figs 10(a) and 11 shows snapshots of the post-seismic velocity field at the Earth's surface on rheology models 1 and 2, respectively. The velocity fields produced on the two rheology models have a similar pattern, and the amplitudes are similar for the earliest time period (0.25 yr after the earthquake), but the amplitudes on rheology 2 are much smaller than those on rheology 1 at later times. This reflects the influence of the relatively large steady state asthenosphere viscosity of 10^{19} Pa s on rheology 2, which dominates the relaxation pattern at timescales greater than τ_2 in the asthenosphere, which is 0.23 yr.

© 2006 The Authors, *GJI*, **167,** 397–420
Journal compilation © 2006 RAS

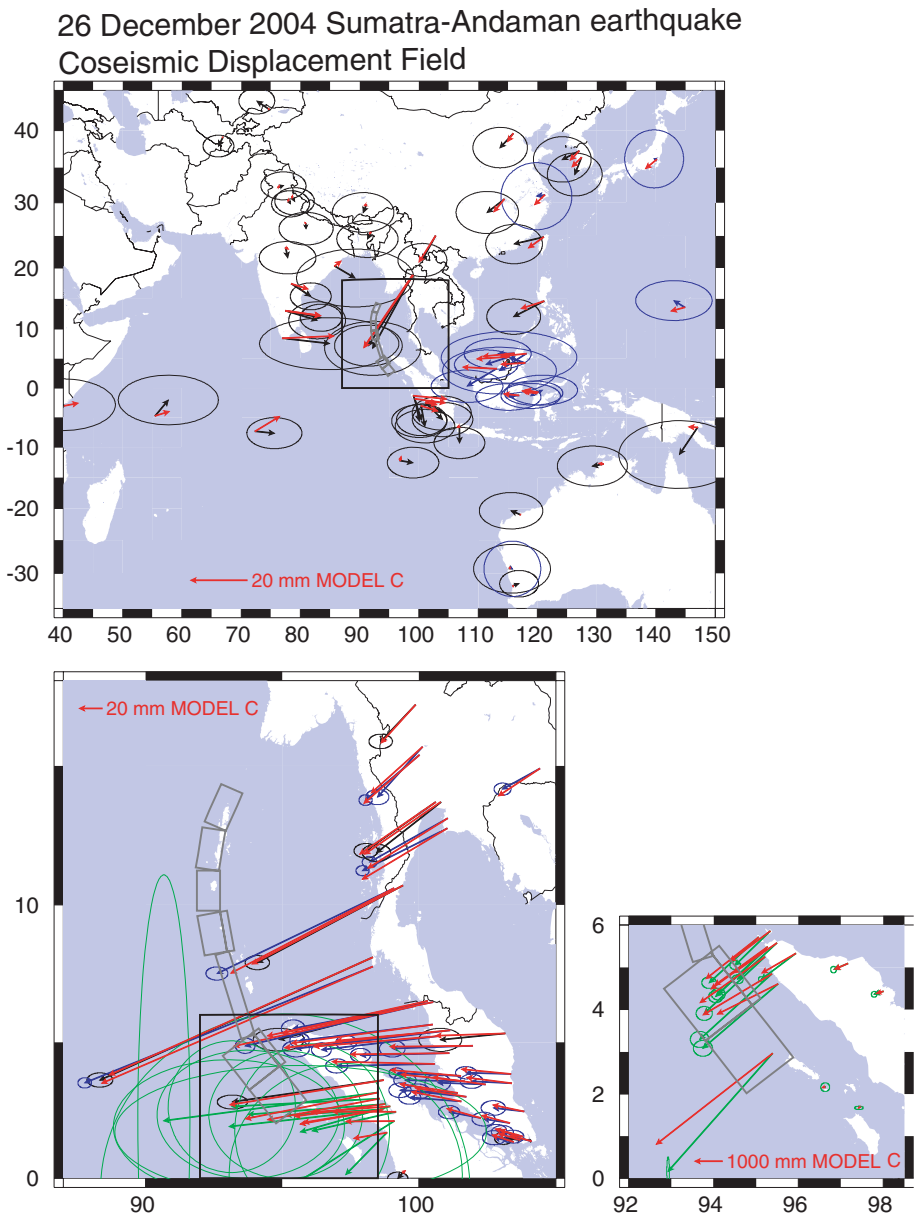

Figure 8. Coseismic horizontal displacement field of the 2004 December 26 earthquake shown by black vectors with 95 per cent error ellipses, together with the 'corrected' coseismic offsets derived from Tables 1 and 2 of Vigny *et al.* (2005), shown by the blue vectors, and coseismic offsets derived from campaign GPS from Table S1 of (Subarya *et al.* 2006), shown by the green vectors. Superimposed red vectors are the predicted static displacements on the PREM model using slip Model C of Banerjee *et al.* (2006). Grey lines indicate the fault planes used to obtain Model C.

The inclusion of gravity in the formulation of post-seismic relaxation is important because it affects the relaxation times and eigenfunctions of all modes. Post-seismic velocities in the gravitational case are generally very close to the corresponding non-gravitational velocities during the early phase of relaxation but become relatively small at times greater than about 8–10 material relaxation times (Pollitz 1997). We examine the effect of gravity on post-Sumatra relaxation by comparing the post-seismic velocity fields calculated with and without gravitational effects. Fig. 10(b) shows the rheology model 1 post-seismic displacement field in the non-gravitational case. The gravitational response in Fig. 10(a) is very close to the non-gravitational response at the earliest two time periods, but is systematically smaller at greater elapsed times. These differences are plotted directly in Fig. 10(c), which indicates generally about 3 per cent smaller gravitational response in the earliest time period (0.25 yr after the earthquake) increasing to about 15 per cent smaller response in the later time period (4 yr after the earthquake). Fig. 10(d) shows the first 10 yr post-seismic response at 6.90°N, 98.62°E generated by the 2004 December 26 source for the westward and downward components. It shows that rheology models 1 and 2 (both with gravity) have almost identical post-seismic velocity immediately after the earthquake, but diverge quickly thereafter. The retarding effect of gravity on post-seismic relaxation increases gradually with time, reaching about −20 per cent for the horizontal component and about −75 per cent for the vertical component after 10 yr. An set of additional rheology-1 curves in Fig. 10(d) labelled 'approximate gravity' refers to the application of Cowling's approximation to the inclusion of the Earth's self-gravitation. In

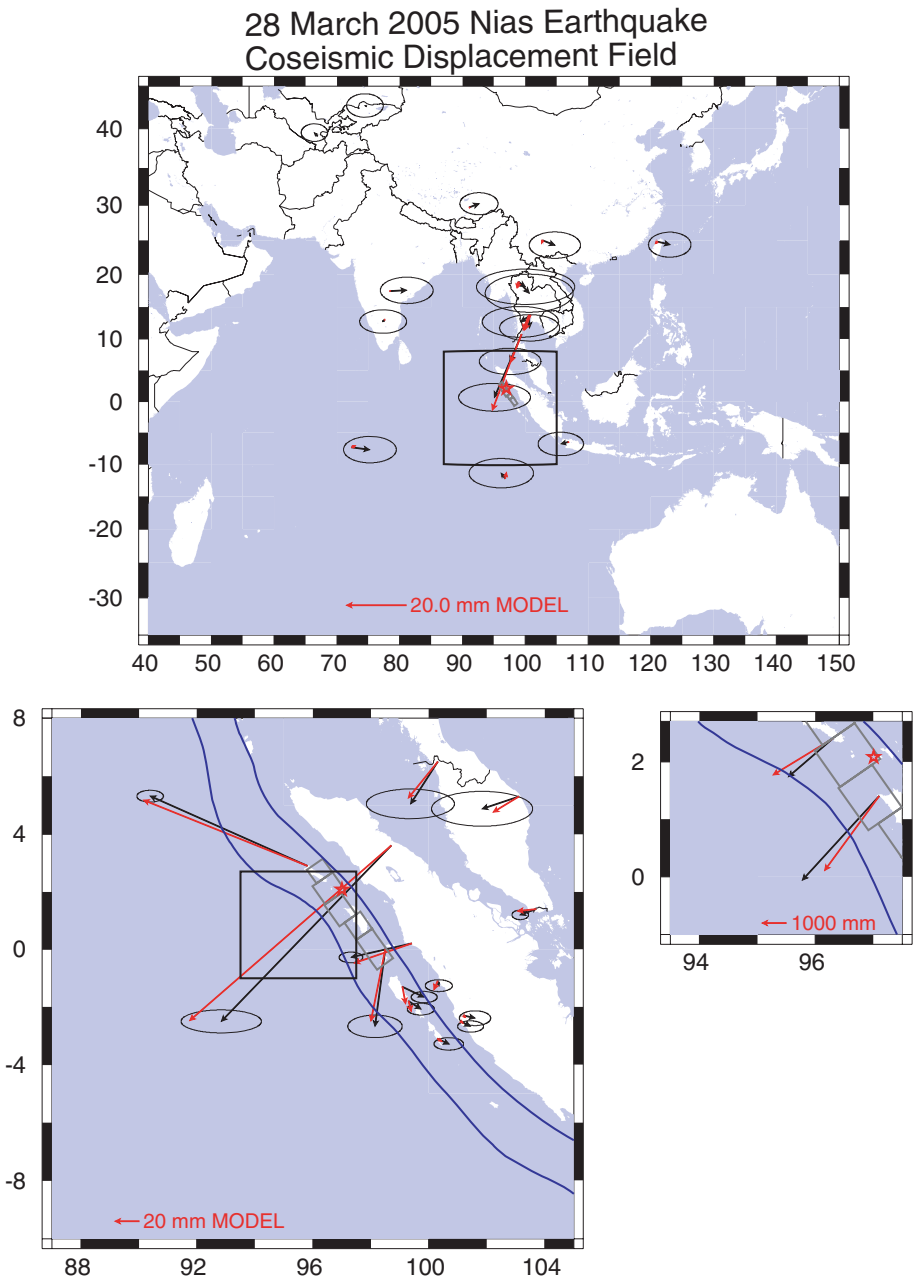

Figure 9. Coseismic displacement field of the 2005 March 28 Nias earthquake at 32 regional GPS sites with 95 per cent errors (Banerjee *et al.* 2006). Superimposed red vectors are the predicted static displacements on the PREM model using a five-plane slip model derived in Banerjee *et al.* (2006). Grey planes indicate the fault planes. Dark blue curves are the 0 and 50 km slab depth contours of Gudmundsson & Sambridge (1998).

this approximation, coupling of changes in the Earth's gravitational potential with the deformation field are neglected, equivalent to including the *g*-terms but neglecting the *G*-terms in the equations of quasi-static equilibrium. Except on the vertical component at very early times, there is negligible difference between the full-gravity and approximate-gravity cases during the time period examined.

Time-series at selected regional GPS sites with strong post-seismic signals are shown in Fig. 12. They were obtained by processing of raw time-series from four regional networks (Fig. 1) in the ITRF2000 reference frame; further details are provided in Pollitz *et al.* (2006). These time-series exhibit clear coseismic offsets at the times of the 2004 December and 2005 March earthquakes, occurring on days 360 and 452, respectively. Most time-series also exhibit a post-seismic transient of up to $\approx$50 cm yr^{-1} during the three months between the two earthquakes. The magnitude and direction of the post-seismic transients agree with the predictions of the viscoelastic models (Figs 10 and 11). This is verified in detail by comparison with predicted time-series on rheology models 1 and 2, shown in Figs 12 and 13, respectively.

4 DISCUSSION

Between the two candidate rheologies, rheology 2 better captures the evolution of regional post-seismic movements during the three months between the 2004 December and 2005 March earthquakes.

© 2006 The Authors, *GJI*, **167,** 397–420
Journal compilation © 2006 RAS

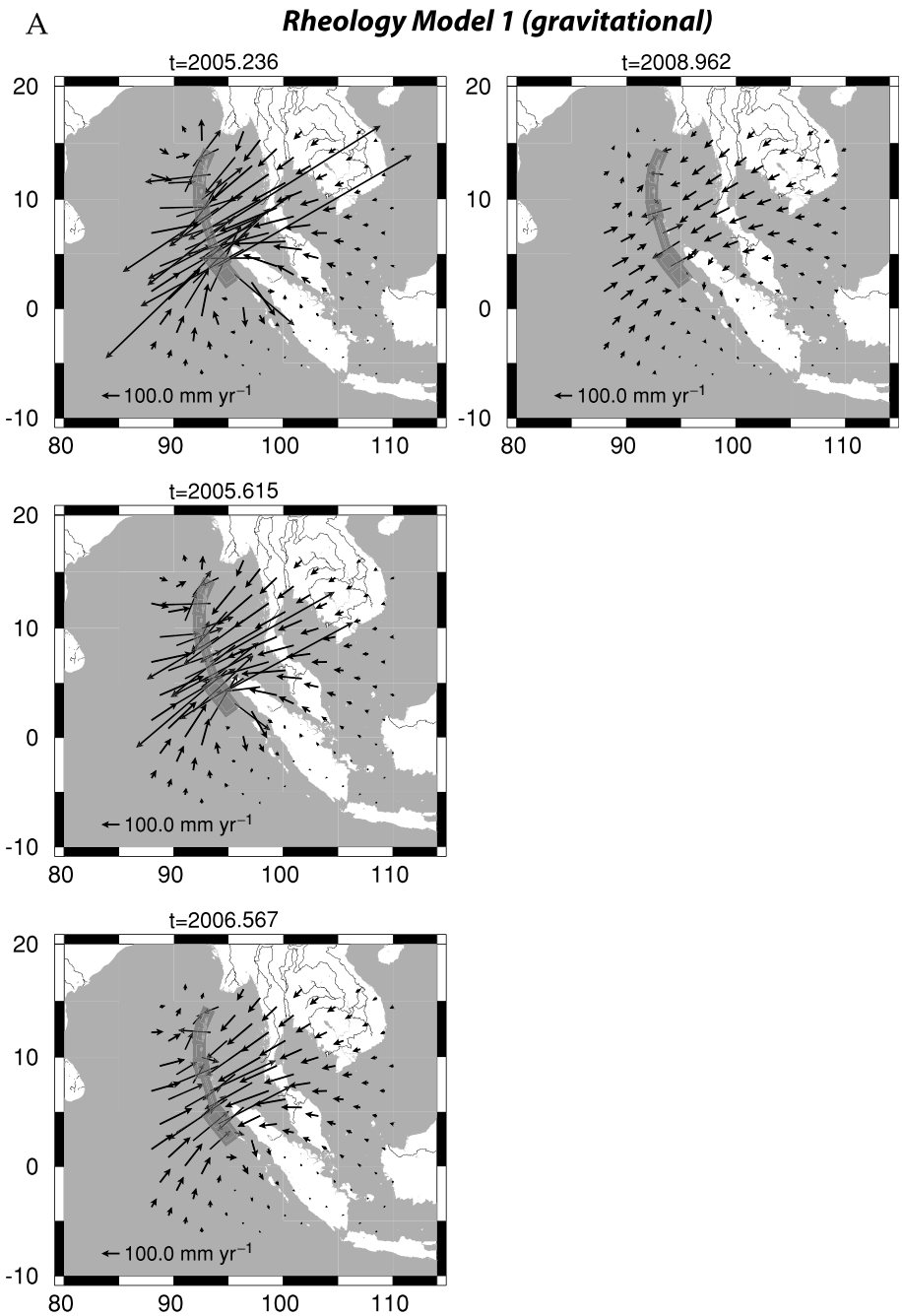

Figure 10. (a) Post-seismic velocity field at Earth's surface (gravitational case) at selected times following the 2004 December 26 Sumatra earthquake. We use rheology model 1 (Fig. 3), which has a Maxwell rheology in the asthenosphere, and coseismic fault Model C of Banerjee *et al.* (2006). (b) Rheology model 1 post-seismic velocity field in the non-gravitational case. (c) Differences between non-gravitational (b) and gravitational (a) post-seismic velocity fields. (d) Westward and downward components of post-seismic velocity fields on rheology 1 (with or without gravity) and rheology 2, at 6.14°N, 100.14°E as a function of time after the 2004 December 26 earthquake. The 'approximate gravity' case for rheology 1 is calculated using the method of Pollitz (1997), which includes the *g*-terms but neglects the *G*-terms in the equations of quasi-static equilibrium. Lower plots are close-ups of the upper plots during the first year.

For the various velocity components shown in Fig. 13, the rheology-2 displacement curves well match the initial post-seismic velocity and curvature during the first three months post-seismic period. This is particularly evident at PHKT and CPN, but it is true for the other time-series as well.

It is useful to obtain simple quantitative measures of the post-seismic time-series in order to better compare the observed time-series with the model predictions. We choose the initial post-seismic velocity and curvature as our measures. For a given time-series we seek to obtain the best-fitting quadratic function

$$u(t) = u_0 + vt + \varsigma t^2, \tag{1}$$

where $u(t)$ is the synthetic time-series beginning at time $t = 0$ (corresponding to the time just after the 2004 December 26 event), v is the initial post-seismic velocity, and ς is the curvature. The three quantities u_0, v, and ς may be calculated exactly for a model time-series;

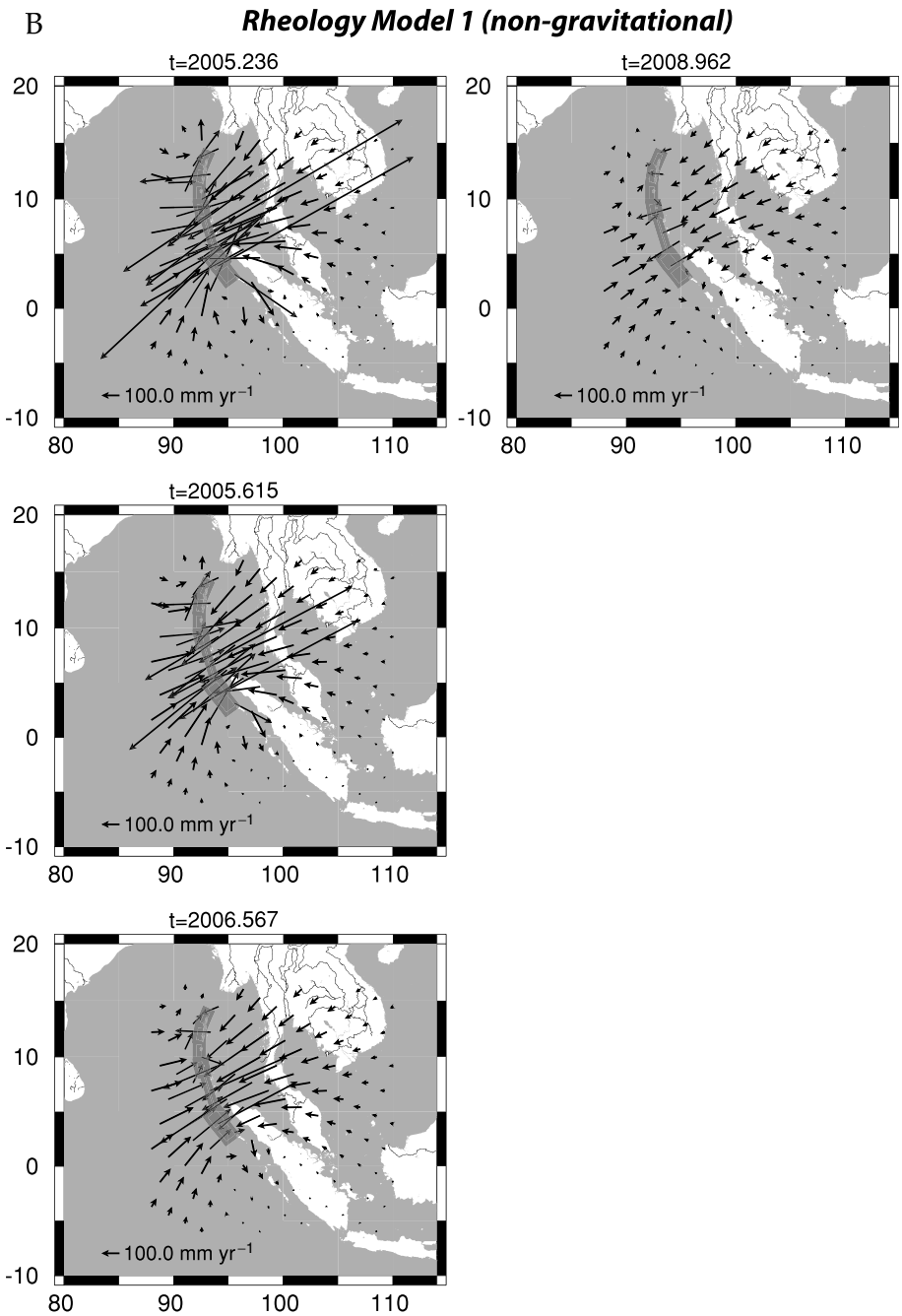

Figure 10. (*Continued.*)

v and ς are the slope evaluated at time $t = 0$ and curvature averaged over the three months between the two events, respectively. The three quantities are estimated from the observed time-series by fitting the observed time-series to $u(t)$ between the times of the 2004 December 26 and 2005 March 28 events. The three unknown parameters are obtained through least-squares inversion, and propagation of data errors yields corresponding standard deviations in these parameters. Fig. 14 shows estimated v and ς for the 20 time-series, together with the corresponding model predictions on rheology models 1 and 2. Fig. 15 presents the same comparisons among data and rheology-model predictions in terms of the horizontal vector representations of v and ς. Both models yield calculated v in excellent agreement with observed v. However, rheology 2 better matches the curvatures of virtually all observed time-series. The improvement is most visible at PHKT and CPN, but it is also significant at SAMP and KMI. This is verified by quantitative evaluation of misfit. For a Burgers body model with variable parameters η_1, η_2, and μ_2, we define the reduced χ^2 fits of calculated to observed velocity and curvature at the GPS sites through

$$\chi_v^2 = \frac{1}{2I-3}\sum_i^I \left(\frac{v_{\rm obs}^i - v_{\rm cal}^i(\eta_1, \eta_2, \mu_2)}{\sigma_v^i}\right)^2$$

$$\chi_\varsigma^2 = \frac{1}{2I-3}\sum_i^I \left(\frac{\varsigma_{\rm obs}^i - \varsigma_{\rm cal}^i(\eta_1, \eta_2, \mu_2)}{\sigma_\varsigma^i}\right)^2, \qquad (2)$$

where I is the number of sites, the index i spans East and North components of site i, and σ_v^i and σ_ς^i are the associated standard deviations in $v_{\rm obs}^i$ and $\varsigma_{\rm obs}^i$, respectively. Rheology model 1 yields

© 2006 The Authors, *GJI*, **167,** 397–420
Journal compilation © 2006 RAS

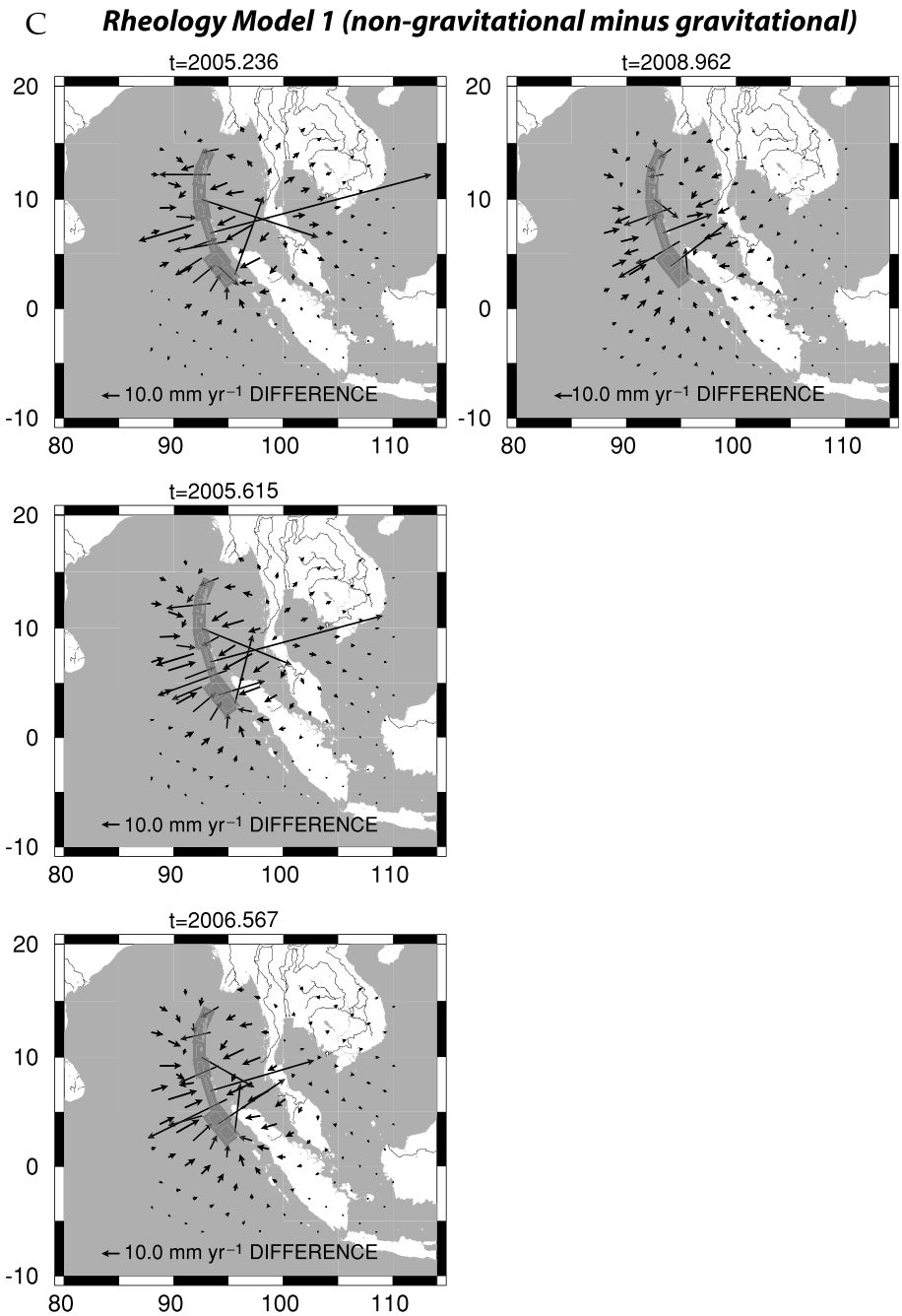

Figure 10. (*Continued.*)

$\chi_v^2 = 2.09$ and $\chi_\varsigma^2 = 5.92$, and rheology model 2 yields $\chi_v^2 = 2.11$ and $\chi_\varsigma^2 = 1.54$.

The almost identical initial post-seismic velocity predictions of the two rheology models are expected on theoretical grounds. Using the notation of eq. (A4), eq. (2) of Pollitz (2003a) shows that for a constant stress step applied at time $t = 0$, the initial velocity on a Maxwell rheology is inversely proportional to τ_1, and the initial velocity on a Burgers body rheology is inversely proportional to τ_2 when $\tau_1 \gg \tau_2$. The near-equality of predicted initial velocities follows from the fact that τ_1 of rheology 1 equals τ_2 of rheology 2 (Section 4.1).

The essential information contained in the post-seismic time-series is embodied in the parameters two v and ς. The behaviour of the Burgers-body rheology model is similarly embodied by three parameters: η_1, η_2, and μ_2 (assuming that the elastic shear modulus μ_1 is known). Sets of observed $\{v\}$ and $\{\varsigma\}$ effectively constrain two of the three parameters, making it an underdetermined problem. The two better-constrained parameters are the transient viscosity η_2 and transient shear modulus μ_2. There is little sensitivity of either v or ς to steady-state viscosity η_1, as seen in misfit patterns conducted over various parameter ranges (Figs 16a and b). Fig. 16(a) confirms that initial post-seismic velocity v is primarily sensitive to τ_2 (or to η_2 for a fixed μ_2). With fixed $\eta_2 = 5 \times 10^{17}$ Pa s, Fig. 16(b) shows that a good match to ς is obtained with a wide range of η_1. This is because the ~3 months time span of the measurements is too short to constrain this parameter, suggesting that longer

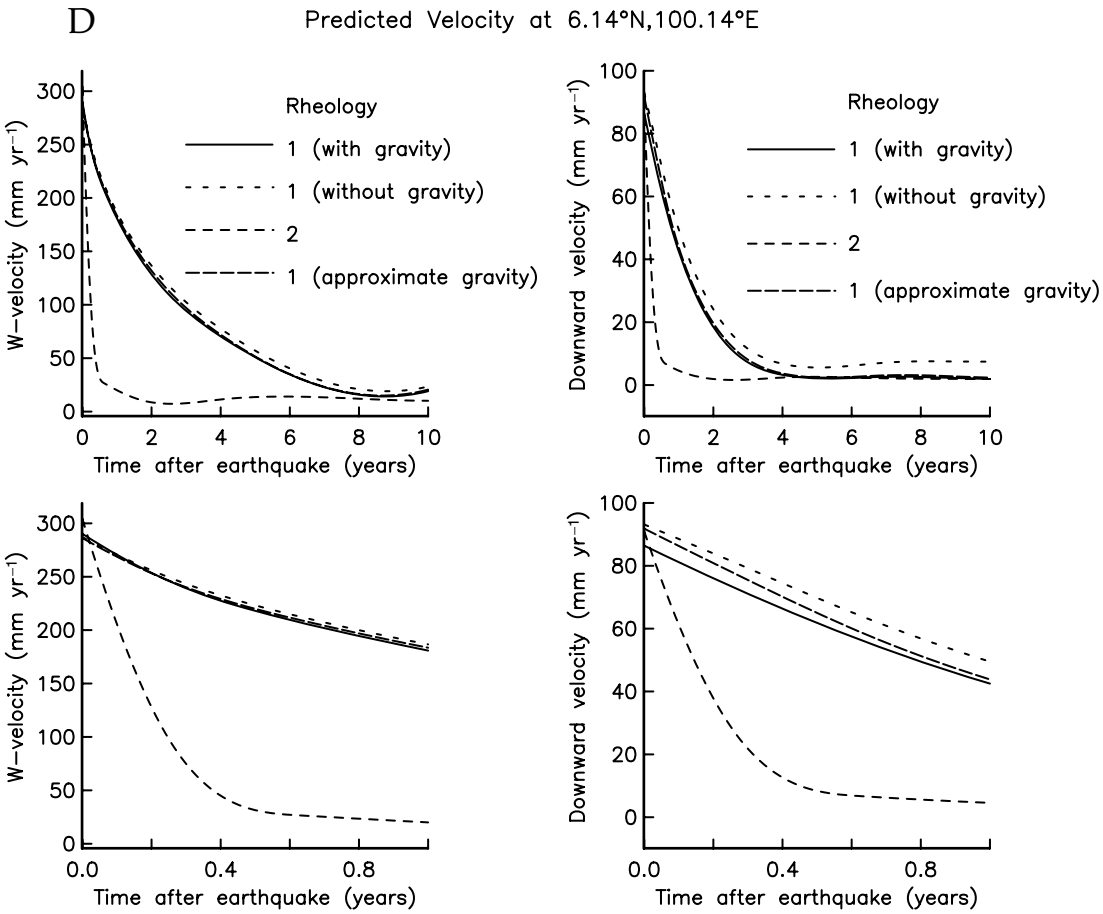

Figure 10. (*Continued.*)

post-seismic time-series are needed to adequately constrain the steady state viscosity. We find negligible sensitivity of initial velocity v but substantial sensitivity of ς to μ_2 (Fig. 16). Fig. 16 suggests that for the chosen values of η_1 and η_2, a value μ_2 near 40 GPa provides the best fit to the post-seismic curvature data, only slightly smaller than the value 33.5 GPa used in rheology model 2.

It is difficult to exploit the signal in vertical GPS measurements because the standard deviation in most daily solutions is of order 20 mm, and strong non-tectonic (i.e. seasonal) signals may also be present. At PHKT, however, the tectonic signal is predicted to be on the order of several cm yr^{-1} subsidence for the early post-seismic period, and the site is positioned in an area of predicted maximal post-seismic subsidence regardless of rheology (Fig. 17). Observed v and ς for the vertical component at PHKT between the 2004 December 26 and 2005 March 28 events is: $v = -11.4 \pm 8.1$ cm yr^{-1} and $\varsigma = 26.9 \pm 31.6$ cm yr^{-2}. These quantities are $v = -22.7$ cm yr^{-1} and $\varsigma = 9.8$ cm yr^{-2} on rheology 1 and $v = -21.8$ cm yr^{-1} and $\varsigma = 33.5$ cm yr^{-2} on rheology 2. Although the estimated signal is marginally significant, this comparison again favours rheology 2.

Our analysis has assumed a laterally homogeneous viscoelastic structure most appropriate for an oceanic environment. It neglects the influence of the downgoing Indo-Australian slab as well as the presence of continental structure east of the subduction zone. The results presented here would be substantially modified if the downgoing slab acted as a strong boundary to viscous mantle flow or if the continental asthenosphere behaved much differently from the oceanic asthenosphere. The predictive power of the viscoelastic model would be strengthened if it could be tested against oceanward observations of post-seismic relaxation, for example, through ocean-bottom GPS.

Afterslip models designed to explain the rapid GPS-constrained post-seismic movements are certainly possible but not required to explain regional post-seismic movements. Hashimoto *et al.* (2006) have constructed a time-dependent afterslip distribution involving continued slip along the Sumatra-Andaman rupture zone during the three months between the 2004 December 26 and 2005 March 28 earthquakes, amounting to about 1 to 3 m total afterslip. It fits a subset of the presented time-series very well. At this stage it is difficult to discriminate between the afterslip and viscoelastic relaxation processes. Detailed observations of post-seismic GPS time-series from the Andaman and Nicobar Islands, to be considered in the future, will greatly help resolve this issue.

Poroelasticity has been convincingly proposed as an important post-seismic mechanism within 3 to 4 km of a strike-slip fault (Jónsson *et al.* 2003), in accordance with expectations based on permeability as a function of depth. At greater distance from the source fault, its effects are expected to diminish rapidly not only because of increasing permeability with depth but also because dilatational strain changes diminish rapidly with distance r (i.e. with a theoretically $1/r^3$ dependence). Forward calculations of post-seismic deformation following a large dip-slip event show that poroelastic rebound is very localized near the source and of much smaller magnitude than viscoelastic relaxation at greater than ∼20 km distance (Masterlark *et al.* 2001).

© 2006 The Authors, *GJI*, **167,** 397–420
Journal compilation © 2006 RAS

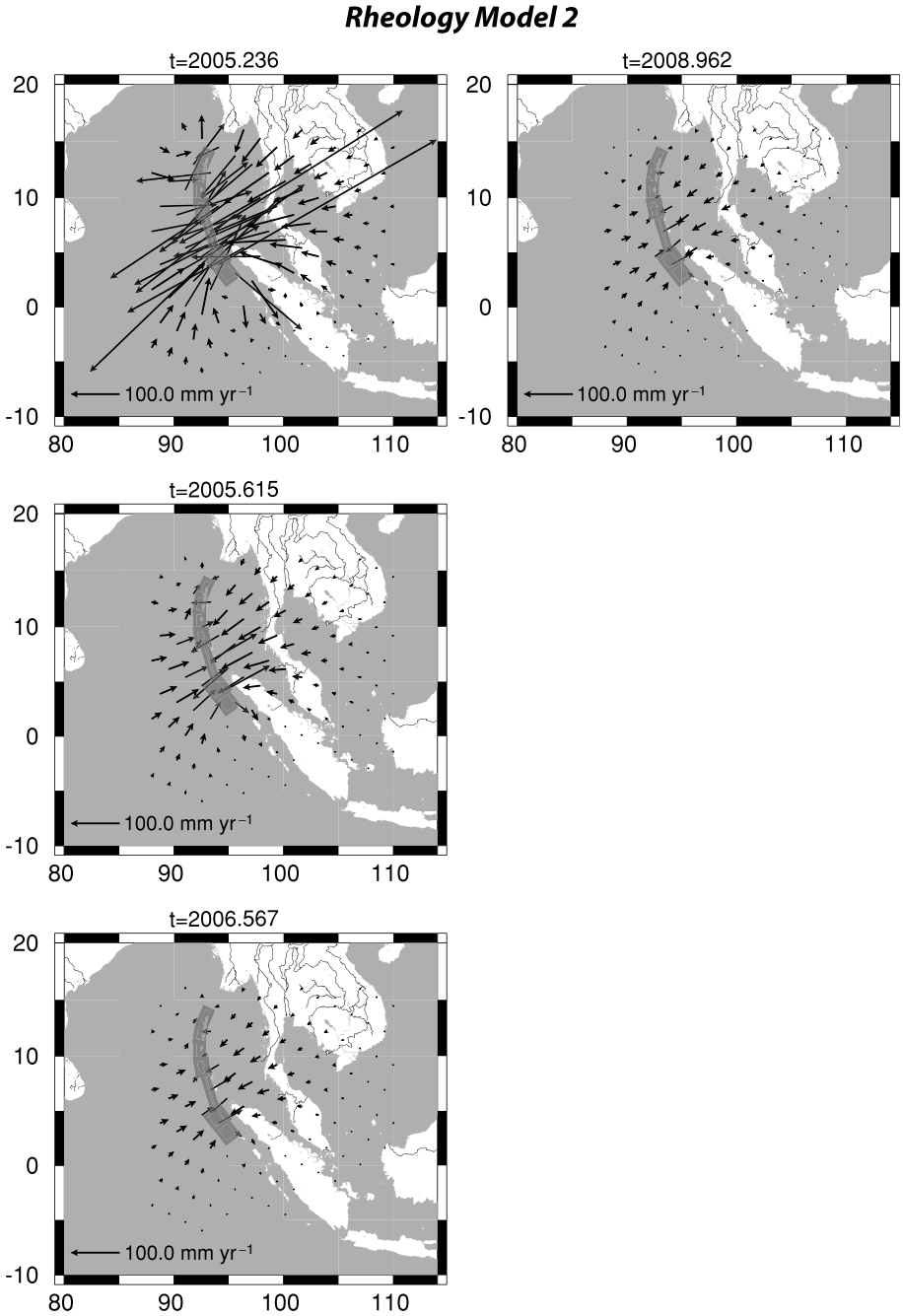

Figure 11. Post-seismic velocity field at Earth's surface (gravitational case) at selected times following the 2004 December 26 Sumatra earthquake. We use rheology model 2 (Fig. 6), which has a Burgers body rheology in the asthenosphere, and coseismic fault Model C of Banerjee *et al.* (2006).

Continued observations of regional displacements may potentially provide greater insight into asthenosphere and deeper mantle rheology. The time-series extrapolated to 10 yr beyond the 2004 Sumatra earthquake in Figs 12 and 13 emphasize the large departure of one rheology from the other after just a few months. It also raises the possibility that with longer post-seismic time-series at hand, one may be able to discriminate additional relaxation times. The characterization of the asthenosphere as a Burgers body with two material time constants is likely an oversimplification. The asthenosphere, as well as the rest of the mantle, may have a continuous spectrum of relaxation times as proposed by Yuen & Peltier (1982) Their composite rheology model combines the behaviour of the absorption band model, which explains seismic wave attenuation, with steady state relaxation which is needed to allow long-term mantle convection. Viscosities of $\approx 10^{20}$ to 10^{21} Pa s are thought to characterize most of the upper and lower mantle (King 1995), and post-seismic time-series extending several years into the future may detect relaxation of material at corresponding depths.

5 CONCLUSIONS

The large dimensions of the 2004 Sumatra-Andaman earthquake have motivated the present treatment of post-seismic relaxation, which is based on viscoelastic relaxation on a self-gravitating,

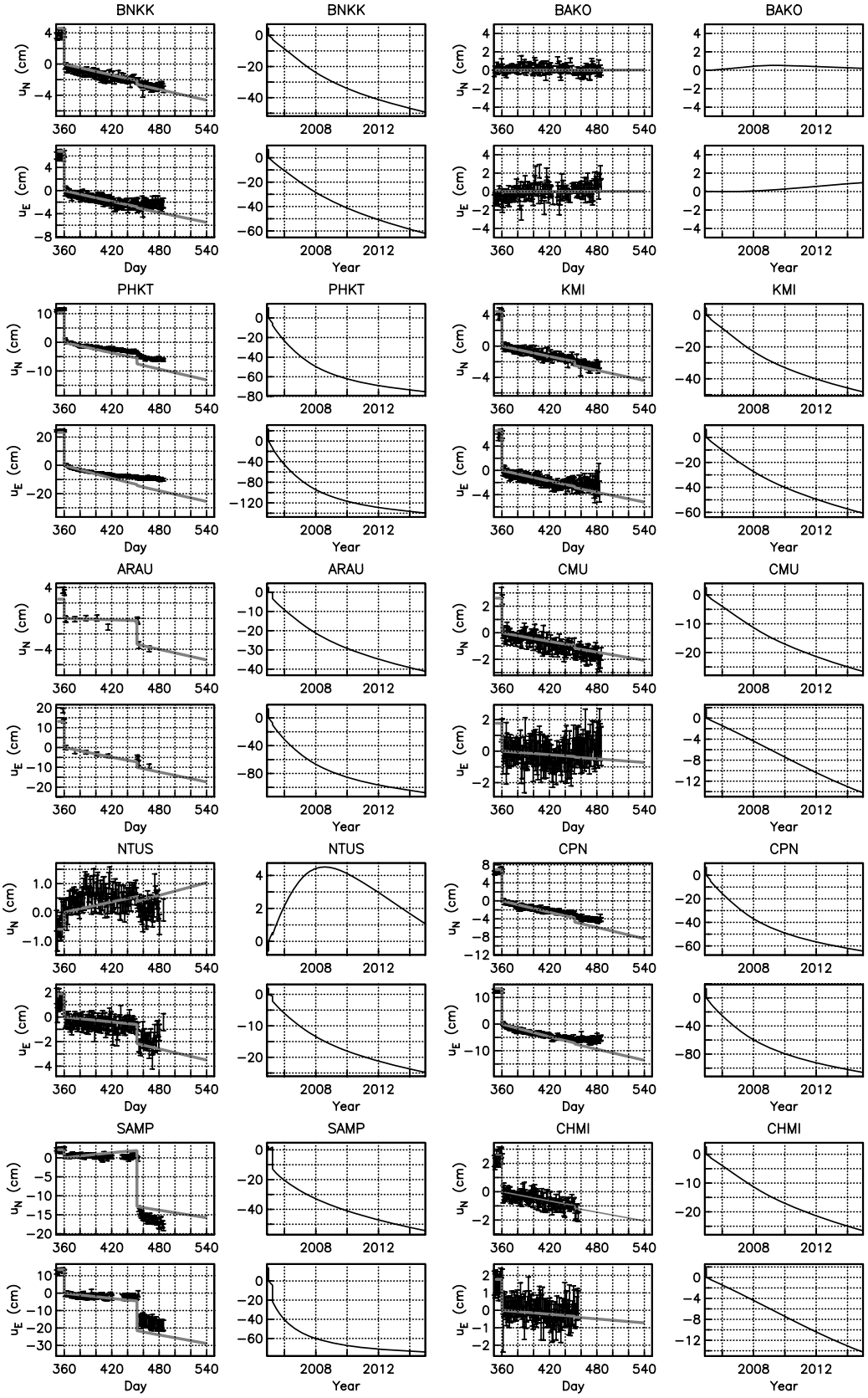

Figure 12. Left-hand side panels: Observed GPS time-series following the 2004 December 26 earthquake with 1-σ errors at selected continuous GPS sites; site locations are shown in Fig. 1. u_E and u_N refer to east- and northward displacement, respectively. Day numbers refer to the year 2004. Superimposed are the predicted displacement curves on rheology 1 that include the effects of coseismic and post-seismic offsets due to the 2004 December 26 and 2005 March 28 Sumatra earthquakes. Right-hand side panels: Predicted time-series extended out to 10 yr beyond the 2004 December 26 earthquake.

© 2006 The Authors, *GJI*, **167,** 397–420
Journal compilation © 2006 RAS

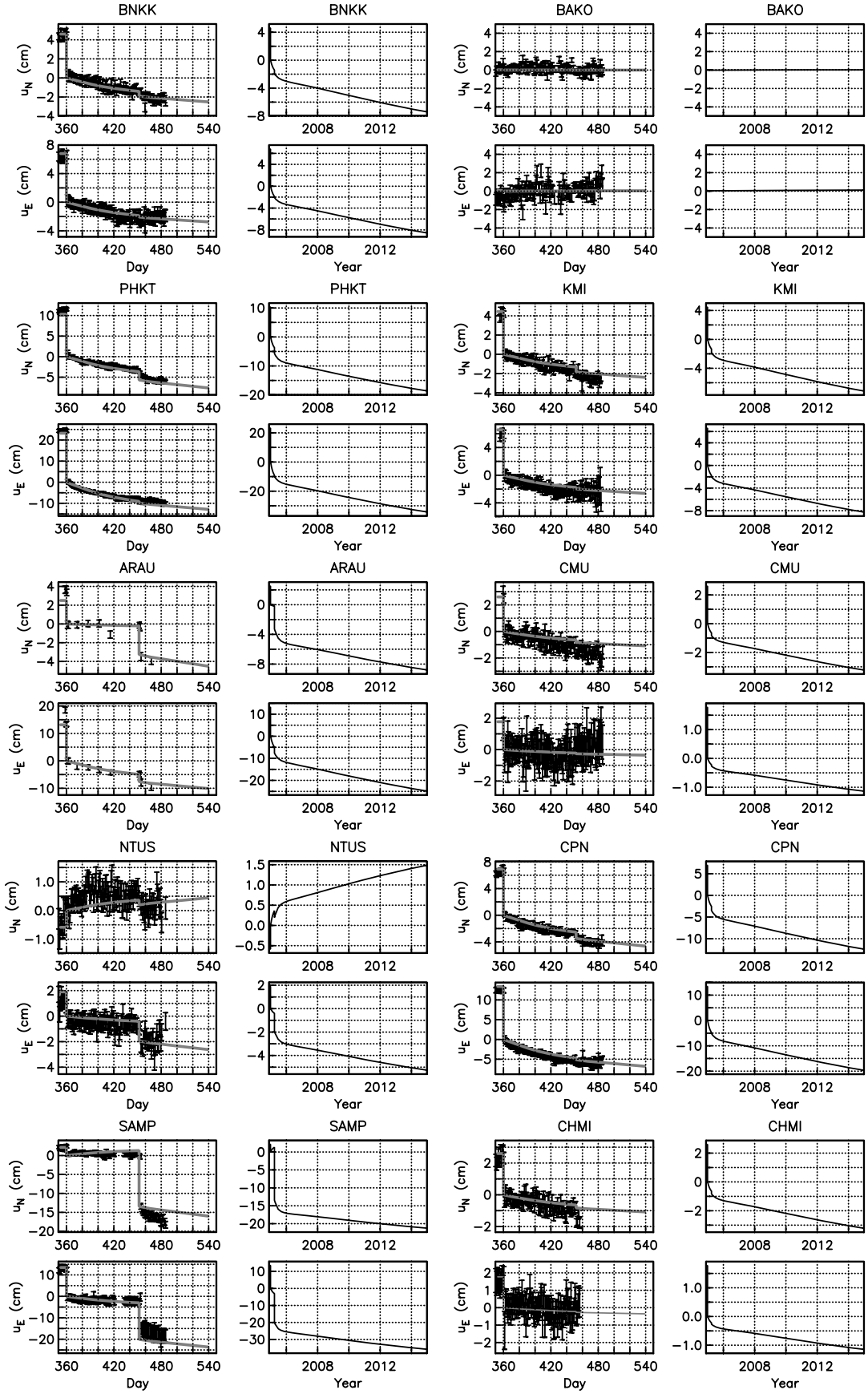

Figure 13. Same comparison as in Fig. 12, but with model time-series calculated on rheology 2.

© 2006 The Authors, *GJI*, **167,** 397–420
Journal compilation © 2006 RAS

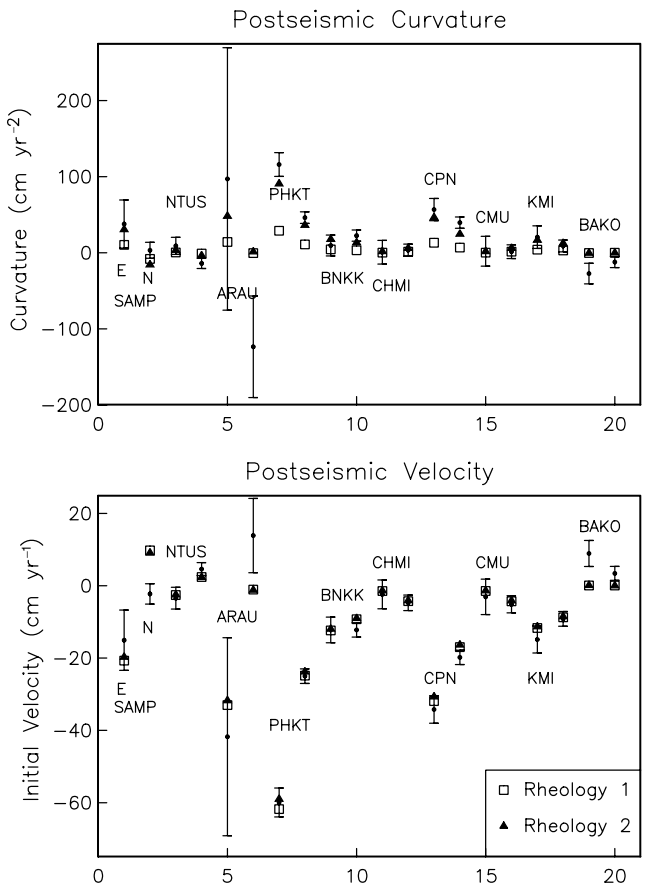

Figure 14. Initial post-seismic velocity v and curvature ς of observed time-series from just after the 2004 December 26 event to just before the 2005 March 28 event, shown with ± 1 standard deviation. Results for the East and North components are shown together for every site label (as indicated for SAMP, for example). Superimposed are the predicted v and ς of the same time-series components from rheology models 1 and 2.

compressible earth model. 20 post-seismic GPS time-series beginning before 2004 December 26 and spanning several months following the 2004 December earthquake exhibit rapid post-seismic velocities of order 10 to 50 cm yr^{-1}. They are interpreted in terms of a combination of coseismic offsets associated with the 2004 December 26 and 2005 March 28 earthquakes and viscoelastic relaxation of the asthenosphere. We consider two candidate rheologies, one involving a low-viscosity asthenosphere with Maxwell rheology, the other involving a Burgers body rheology with low transient viscosity in the asthenosphere. The Burgers body rheology satisfactorily explains both the initial post-seismic velocity and curvature of practically all time-series between the times of the two events. This lends support to the notion that flow of high-temperature rock is characterized by more than one material relaxation time.

ACKNOWLEDGMENTS

We greatly appreciate data made available by BAKOSURTANAL (SAMP), IGS (BAKO, NTUS), the Department of Survey and Mapping Malaysia (MASS sites), Prof. Narong Hemmakorn at the King Monkut's Institute of Technology Ladkrabang, Thailand (CPN, KMI), Prof. Tharadol Komolmis, Chiang Mai University, Thailand (CHMI), Dr Susumu Saito (NICT sites), and the Tectonics Observatory at Caltech, the Indonesian Institute of Sciences (LIPI) and Scripps Orbit and Permanent Array Center (SuGAr network). We also thank Prof. M. Hashizume for his efforts of establishing GPS monitoring stations in Thailand.

REFERENCES

Ammon, C. *et al.*, 2005. Rupure process of the great 2004 Sumatra-Andaman earthquake, *Science,* **308,** 1133–1139.

Banerjee, P., Pollitz, F. & Bürgmann, R., 2005. Size and duration of the great 2004 Sumatra-Andaman earthquake from far-field static offsets, *Science,* **308,** 1769–1772.

Banerjee, P., Pollitz, F. & Bürgmann, R., 2006. Coseismic slip distributions of the 26 December 2004 Sumatra-Andaman earthquake and 28 March 2005 Nias earthquake from GPS static offsets, *Bull. seism. Soc. Am.*, submitted.

Ben-Menahem, A. & Singh, S., 1981. *Seismic waves and sources*, Springer-Verlag, New York.

Cathles, L., 1975. *The viscosity of the Earth's mantle*, Princeton University Press, Princeton, New Jersey.

Dahlen, F., 1972. Elastic dislocation theory for a self-gravitating elastic configuration with an initial static stress field, *Geophys. J. R. astr. Soc.,* **28,** 357–383.

Dahlen, F. & Tromp, J., 1998. *Theoretical Global Seismology*, Princeton University Press, Princeton, New Jersey.

Dziewonski, A. & Anderson, D., 1981. Preliminary reference earth model, *Phys. Earth planet. Inter.,* **25,** 297–356.

Fang, M. & Hager, B., 1995. The singularity mystery associated with a radially continuous Maxwell viscoelastic structure, *Geophys. J. Int.,* **123,** 849–865.

Freymueller, J., Cohen, S. & Fletcher, H., 2000. Spatial variations in present-day deformation, Kenai Peninsula, Alaska, and their implications, *J. geophys. Res.,* **105,** 8097–8101.

Gaherty, J., Jordan, T. & Gee, L., 1996. Seismic structure of the upper mantle in a central Pacific corridor, *J. geophys. Res.,* **101,** 22 291–22 309.

Gudmundsson, O. & Sambridge, M., 1998. A regionalized upper mantle (RUM) model, *J. geophys. Res.,* **103,** 7121–7136.

Han, D. & Wahr, J., 1995. The viscoelastic relaxation of a realistically stratified earth, and a further analysis of postglacial rebound, *Geophys. J. Int.,* **120,** 287–311.

Hanyk, L., Matyska, C. & Yuen, D., 1999. Secular gravitational instability of a compressible viscoelastic sphere, *Geophys. Res. Lett.,* **26,** 557–560.

Hashimoto, M., Chhoosakul, N., Hashizume, M., Takemoto, S., Takiguchi, H., Fukada, Y. & Fujimori, K., 2006. Crustal deformations associated with the Great Sumatra-Andaman earthquake deduced from continuous GPS observation, *Earth, Planets, Space,* **58,** 127–139.

Hu, Y., Wang, K., He, J., Klotz, J. & Khazaradze, G., 2004. Three-dimensional viscoelastic finite element model for postseismic deformation of the great 1960 Chile earthquake, *J. geophys. Res.,* **109,** B12403, doi:10.1029/2004JB003163.

Ji, C., 2005. Updated result of the 05/03/28 (Mw 8.5), Sumatra earthquake, *http://www.gps.caltech.edu/ jichen/Earthquake/2005/sumatra/sumatra.html*.

Jónsson, S., Segall, P., Pedersen, R. & Björnsson, G., 2003. Post-earthquake ground movements correlated to pore-pressure transients, *Nature,* **424,** 179–183.

King, S., 1995. Models of mantle viscosity, in *Mineral Physics and Crystallography: A Handbook of Physical Constants, AGU Reference Shelf 2*, pp. 227–236, American Geophysical Union, Washington, DC.

Masterlark, T., DeMets, C., Wang, H., Sánchez, O. & Stock, J., 2001. Homogeneous vs heterogeneous subduction zone models: Coseismic and postseismic deformation, *Geophys. Res. Lett.,* **28,** 4047–4050.

Peltier, W., 1974. The impulse response of a Maxwell earth, *Rev. Geophys.,* **12,** 649–669.

Piersanti, A., Spada, G., Sabadini, R. & Bonafede, M., 1995. Global post-seismic deformation, *Geophys. J. Int.,* **120,** 544–566.

Plag, H.-P. & Jüttner, 1995. Rayleigh-taylor instabilities of a self-gravitating earth, *J. Geodyn.,* **20,** 267–288.

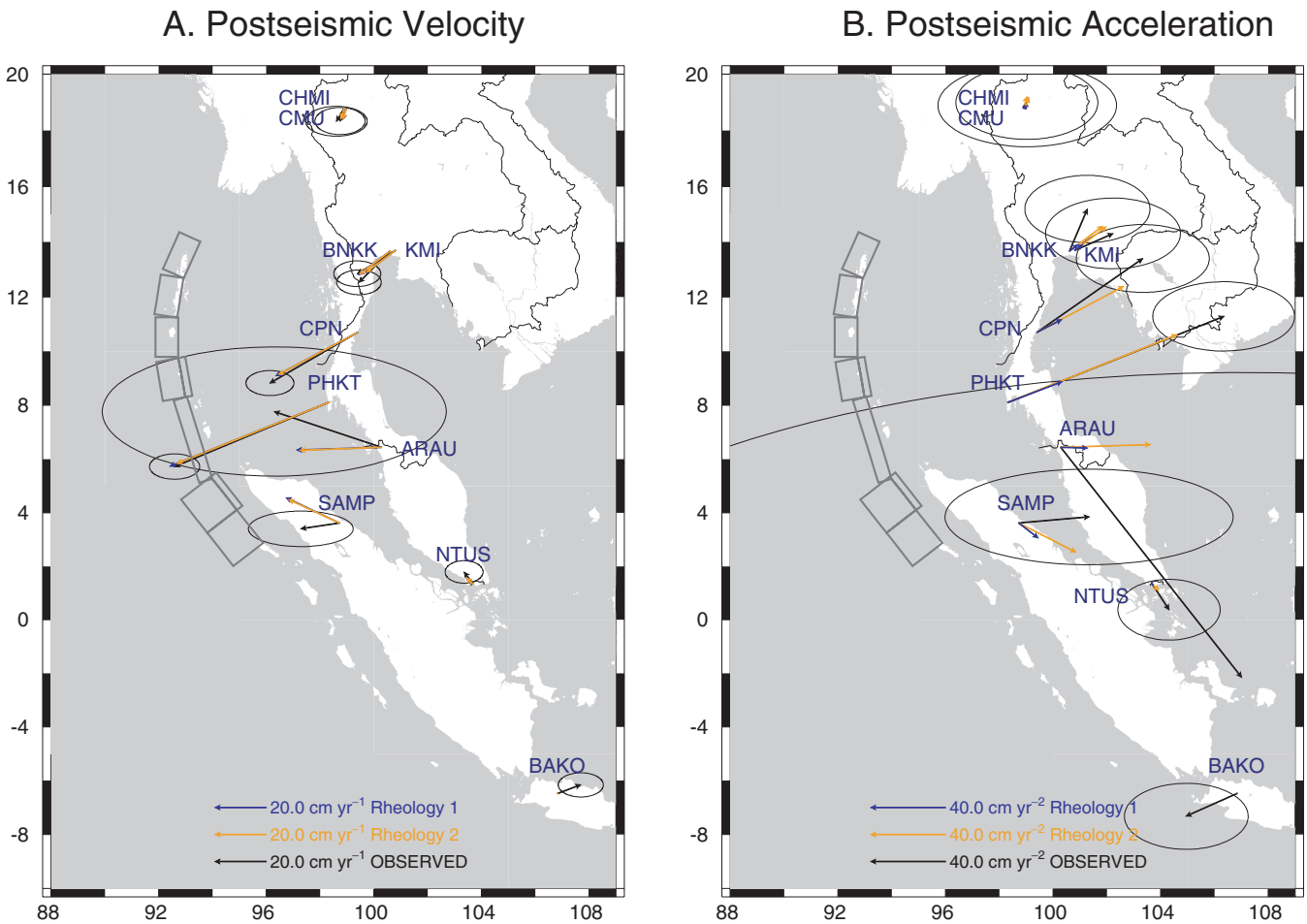

Figure 15. Initial post-seismic velocity v(a) and curvature ς(b) of observed time-series, shown with 95 per cent error ellipses, and predicted v and ς on rheology models 1 and 2, all corresponding to the time from just after the 2004 December 26 event to just before the 2005 March 28 event.

Pollitz, F.F., 1992. Postseismic relaxation theory on a layered spherical earth, *Bull. seism. Soc. Am.,* **82,** 422–453.

Pollitz, F.F., 1996. Coseismic deformation from earthquake faulting on a layered spherical earth, *Geophys. J. Int.,* **125,** 1–14.

Pollitz, F.F., 1997. Gravitational viscoelastic postseismic relaxation on a layered spherical earth, *J. geophys. Res.,* **102,** 17 921–17 941.

Pollitz, F.F., 2003a. Transient rheology of the uppermost mantle beneath the Mojave Desert, California, *Earth planet. Sci. Lett.,* **215,** 89–104.

Pollitz, F.F., 2003b. Postseismic relaxation theory on a laterally heterogeneous viscoelastic model, *Geophys. J. Int.,* **155,** 57–78.

Pollitz, F.F., Bürgmann, R. & Romanowicz, B., 1998. Viscosity of oceanic asthenosphere inferred from remote triggering of earthquakes, *Science,* **280,** 26 975–26 992.

Pollitz, F.F., Banerjee, P. & Bürgmann, R., 2006. Stress evolution along the Sunda trench following the 26 December 2004 Sumatra-Andaman and 28 March 2005 Nias earthquakes, *Geophys. Res. Lett.,* **33,** L06309, doi: 10.1029/2005gl024558.

Press, W., Teukolsky, S., Vetterling, W. & Flannery, B., 1996. *Numerical Recipes in Fortran 90, Volume 2*, Cambridge University Press.

Riva, R. & Vermeersen, L., 2002. Approximation method for high-degree harmonics in normal mode modelling, *Geophys. J. Int.,* **151,** 309–313.

Saito, M., 1974. Some problems of static deformation of the earth, *J. Phys. Earth,* **22,** 123–140.

Stein, S. & Okal, E., 2005. Speed and size of the Sumatran earthquake, *Nature,* **434,** 581–582.

Subarya, C. *et al.*, 2006. Plate-boundary deformation of the great Aceh-Andaman earthquake, *Nature,* **440,** 46–51.

Takeuchi, H. & Saito, M., 1972. Seismic surface waves, in *Methods in Computational Physics*, Vol. 11, pp. 217–295, Academic Press, New York.

Vermeersen, L. & Mitrovica, J., 2000. Gravitational instability of spherical self-gravitating relaxation models, *Geophys. J. Int.,* **142,** 351–360.

Vermeersen, L. & Sabadini, R., 1997. A new class of stratified viscoelastic models by analytical techniques, *Geophys. J. Int.,* **129,** 531–570.

Vermeersen, L., Sabadini, R. & Spada, G., 1996. Compressible rotational deformation, *Geophys. J. Int.,* **126,** 735–761.

Vigny, C. *et al.*, 2005. GPS in SE Asia provides unforseen insights on the 2004 megathrust earthquake, *Nature,* **436,** 201–206.

Wolf, D., 1991. Viscoelastodynamics of a stratified compressible planet: incremental field equations and short- and long-time asymptotes, *Geophys. J. Int.,* **104,** 401–417.

Woodhouse, J., 1988. The calculation of eigenfrequencies and eigenfunctions of the free oscillations of the earth and the sun, in *Seismological Algorithms*, pp. 321–370, ed. Doornbos, D., Academic Press.

Wu, P. & Ni, Z., 1996. Some solutions for the viscoelastic gravitational relaxation of a two-layer non-self-gravitating incompressible spherical earth, *Geophys. J. Int.,* **126,** 413–436.

Wu, P. & Peltier, W., 1982. Viscous gravitational relaxation, *Geophys. J. R. astr. Soc.,* **70,** 435–485.

Yuen, D. & Peltier, W., 1982. Normal modes of the viscoelastic Earth, *Geophys. J. R. astr. Soc.,* **69,** 495–526.

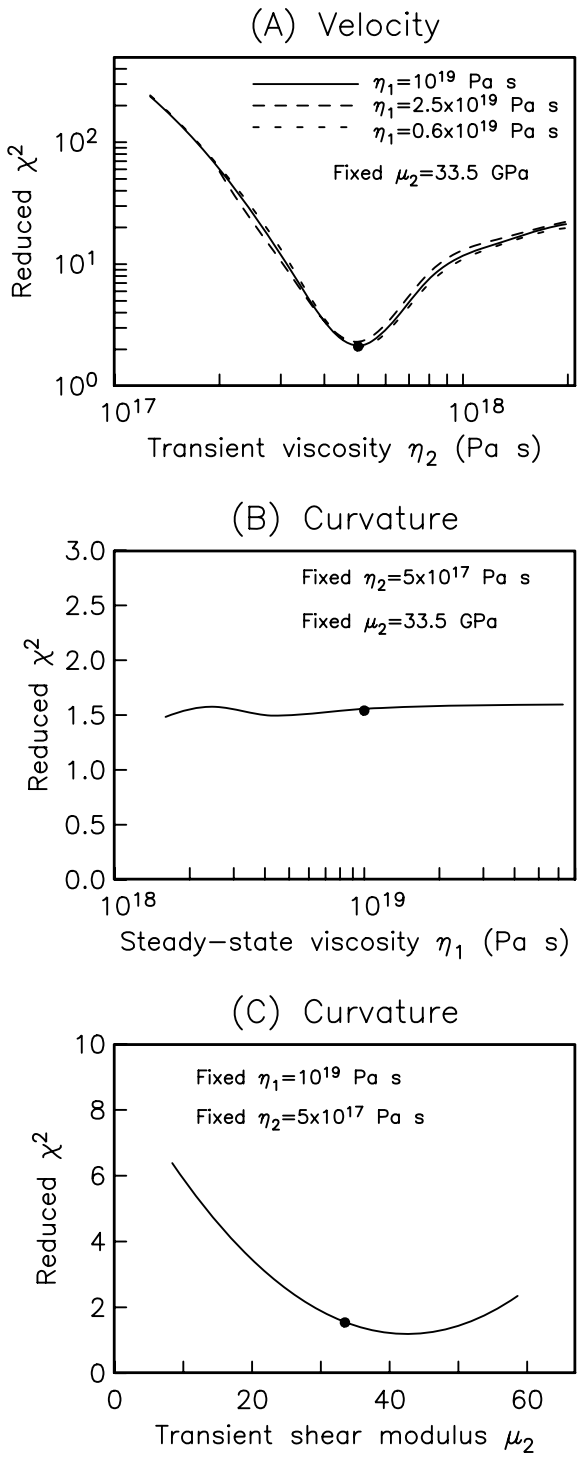

Figure 16. (a) χ_v^2 and (b and c) χ_ς^2 resulting from viscoelastic models with various combinations of η_1, η_2, and μ_2. Note that there is little sensitivity of either v or ς to η_1. Filled circles indicate the fit of rheology model 2.

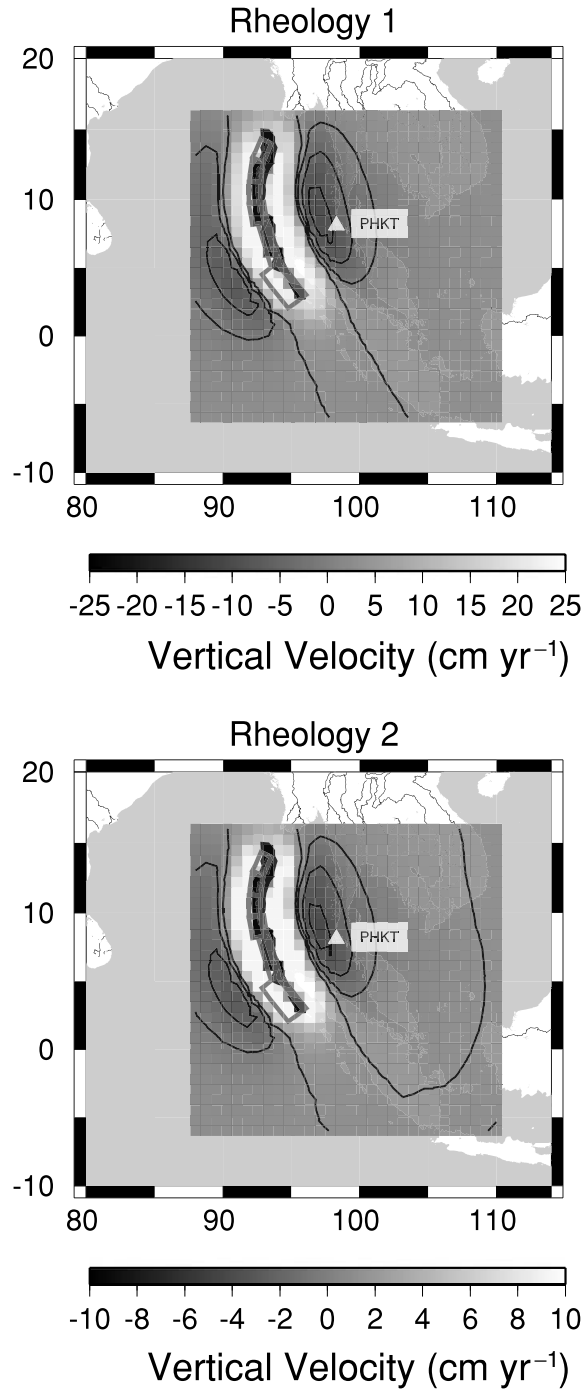

Figure 17. Post-seismic vertical velocity (positive upward) at time 0.25 yr after the 2004 December 26 event at Earth's surface on rheology models 1 and 2. Contour interval for negative velocity (i.e. subsidence) is 5 cm yr^{-1} for rheology model 1 and 2 cm yr^{-1} for rheology model 2.

APPENDIX A: VISCOELASTIC NORMAL MODE REPRESENTATION OF POST-EARTHQUAKE RELAXATION

The theory presented here follows the derivation of Earth's free oscillations presented in many works (e.g. Takeuchi & Saito 1972; Ben-Menahem & Singh 1981; Dahlen & Tromp 1998) and differs mainly in the assumption of zero frequency for the quasi-static problem and the application of the correspondence principle (e.g. Cathles 1975). It is similar to that presented by Peltier (1974), and it is repeated here

in order to emphasize the application to seismic source excitation rather than surface loading. In addition, we intend application of this theory to a Burgers body rheology (Pollitz 2003a), for which the early post-earthquake evolution is very rapid and hence compressibility effects, which are included here, are expected to be important.

Let elastic parameters $\{\mu(r), \kappa\ (r)\}$, density $\rho_0(r)$, and viscosity $\eta(r)$ define a spherically-symmetric, isotropic, non-rotating Earth model in a spherical $r - \theta - \phi$ geometry, where μ, κ, ρ_0, and η are the depth-dependent shear modulus, bulk modulus, density, and viscosity, respectively. Let $\phi_0(r)$ and $p_0(r)$ be the initial gravitational potential and pressure fields, respectively. These are prescribed by

$$\nabla p(\mathbf{r}) = -\rho_0(r)\nabla\phi_0(\mathbf{r}) = -\rho_0(r)g(r)\hat{\mathbf{r}}, \tag{A1}$$

together with Poisson's equation

$$\nabla^2\phi_0 = 4\pi G\rho_0, \tag{A2}$$

where G is the gravitational constant and g is the gravitational acceleration. After an earthquake the Earth moves from its initial state of equilibrium. To describe the time dependence it is convenient to work in the Laplace transform domain. The Laplace transform of a function with dependent variable s is

$$L[f(t)] = \int_0^\infty f(t)\exp(-st)\,dt. \tag{A3}$$

It is assumed that constitutive relation relating tensor strain rate and stress is linear, as is the case for the well-known Maxwell viscoelastic solid, standard linear solid, and Burgers body (e.g. Yuen & Peltier 1982). Viscoelasticity is realized by application of the correspondence principle, through which the elastic parameters are replaced with s-dependent elastic parameters, for example,

$$\mu(r;s) = \mu_1 s\frac{s+\tau_2^{-1}}{\left(s+\tau_2^{-1}\right)\left(s+\tau_1^{-1}\right)+\frac{\mu_1 s}{\eta_2}}, \tag{A4}$$

for a Burgers body. In eq. (A4), the relaxation time $\tau_1 = \frac{\eta_1}{\mu_1}$, where $\eta_1 = \eta(r)$ and $\mu_1 = \mu(r)$ are the steady state viscosity and steady state shear modulus, respectively; the relaxation time $\tau_2 = \frac{\eta_2(r)}{\mu_2(r)}$, where $\eta_2(r)$ and $\mu_2(r)$ are the transient viscosity and transient shear modulus, respectively. We define the transformed perturbed density and gravitational potential at $\mathbf{r} = (r, \theta, \phi)$

$$\begin{aligned}\rho(\mathbf{r}, s) &= \rho_0(r) + \rho_1(\mathbf{r}, s)\\ \phi(\mathbf{r}, s) &= \phi_0(r) + \phi_1(\mathbf{r}, s).\end{aligned} \tag{A5}$$

Let a source with impulsive moment tensor $\mathbf{M}(t) = \mathbf{M}H(t)$ be located at $\mathbf{r}_s$. Denoting the transformed displacement field with $\mathbf{u}(\mathbf{r}, s)$ and the corresponding elastic stress tensor with $\mathbf{T}(\mathbf{r}.\ s)$, the linearized equations of quasi-static equilibrium are

$$-\rho_0\nabla\phi_1 - \rho_1\nabla\phi_0 - \nabla[\rho_0\mathbf{u}\cdot\nabla\phi_0] + \nabla\cdot\mathbf{T} = \frac{1}{s}\mathbf{M} : \nabla\delta(\mathbf{r}-\mathbf{r}_s), \tag{A6}$$

$$\rho_1 = -\nabla\cdot(\rho_0\mathbf{u}), \tag{A7}$$

$$\nabla^2\phi_1 = 4\pi G\rho_1, \tag{A8}$$

$$\mathbf{T} = \kappa(\nabla\cdot\mathbf{u})\mathbf{I} + 2\mu\left[\epsilon - \frac{1}{3}(\nabla\cdot\mathbf{u})\mathbf{I}\right]. \tag{A9}$$

In eq. (A9) ϵ is the strain tensor

$$\epsilon = \frac{1}{2}[(\nabla\mathbf{u}) + (\nabla\mathbf{u})^T], \tag{A10}$$

and $\mathbf{I}$ is the identity matrix. Eqs (A6) to (A8) are the transformed eqs (11) and (12) of Dahlen (1972) without the inertial, rotational, or initial stress deviator terms. Eq. (A9) is the stress–strain relation for an isotropic material.

In the normal mode method, eqs (A6) to (A10) are first solved without the forcing term, and the solutions of the forced system are represented in terms of a sum of modes with excitation coefficients which depend on $\mathbf{M}$ and the source depth (e.g. Pollitz 1997). The normal modes are found by representing the solution to the unforced system as a superposition of spherical harmonics. The equations decouple into separate systems of equations for toroidal and spheroidal motion solutions and are separable in spherical harmonic degree. In the case of toroidal motion, displacement and traction are represented as

$$\mathbf{u}(\mathbf{r}, s) = -y_1(r, s)\,[\hat{\mathbf{r}}\times\nabla_1]\,Y_l(\hat{\mathbf{r}}), \tag{A11}$$

$$\hat{\mathbf{r}}\cdot\mathbf{T}(\mathbf{r}, s) = -y_2(r, s)\,[\hat{\mathbf{r}}\times\nabla_1]\,Y_l(\hat{\mathbf{r}}), \tag{A12}$$

where $\nabla_1 = (\frac{\partial}{\partial\theta} + (\sin\theta)^{-1}\frac{\partial}{\partial\phi})$ is the surface gradient operator and Y_l represents a spherical harmonic of degree l. The components y_1 and y_2 of the displacement-stress vector are the horizontal displacement and shear traction on a spherical shell of radius r, respectively. Substitution of eqs (A11) and (A12) into eqs (A6) to (A10) yields

$$\begin{aligned}
\mathbf{y} &= [\,y_1 \quad y_2\,]^T \\
\frac{d\mathbf{y}}{dr} &= \mathbf{A}\cdot\mathbf{y} \\
\mathbf{A} &= \begin{pmatrix} r^{-1} & \mu^{-1} \\ r^{-2}\mu(L-2) & -3r^{-1} \end{pmatrix},
\end{aligned} \tag{A13}$$

where

$$\begin{aligned}
\mu &= \mu(r,s) \\
L &= l(l+1).
\end{aligned} \tag{A14}$$

The system of coupled first-order differential equations A12 is to be integrated from the Earth's interior to the surface subject to continuity of the two functions y_1 and y_2. If the starting radius of integration is taken to be the core–mantle boundary at radius b, then there is one independent solution at that radius given by

$$\mathbf{y}^I(b,s) = \begin{pmatrix} 1 \\ 0 \end{pmatrix}. \tag{A15}$$

Admissible solutions must satisfy vanishing traction at Earth's surface at radius a:

$$\hat{\mathbf{r}}\cdot\mathbf{T}(a,s) = \mathbf{0}, \tag{A16}$$

or equivalently

$$y_2^I(a,s) = 0. \tag{A17}$$

In the case of spheroidal motion, displacement, traction, and perturbed gravitational potential are represented as

$$\mathbf{u}(\mathbf{r},s) = [y_1(r,s)\hat{\mathbf{r}} + y_3(r,s)\nabla_1]\,Y_l(\hat{\mathbf{r}}), \tag{A18}$$

$$\hat{\mathbf{r}}\cdot\mathbf{T}(\mathbf{r}) = [y_2(r,s)\hat{\mathbf{r}} + y_4(r,s)\nabla_1]\,Y_l(\hat{\mathbf{r}}), \tag{A19}$$

$$\phi_1 = y_5(r,s)Y_l(\hat{\mathbf{r}}). \tag{A20}$$

The components $y_1,\ldots,y_4$ of the displacement-stress vector are: vertical displacement, normal traction on a spherical shell of given radius r, horizontal displacement, and shear traction on the spherical shell, respectively. Following Saito (1974) we further define an auxiliary function y_6 by

$$\frac{d\phi_1}{dr} - 4\pi G\rho\hat{\mathbf{r}}\cdot\mathbf{u} + \frac{l+1}{r} = y_6(r,s)Y_l(\hat{\mathbf{r}}). \tag{A21}$$

Substitution of eqs (A18) to (A21) into eqs (A6) to (A10) yields

$$\begin{aligned}
\mathbf{y} &= \begin{bmatrix} y_1 & y_2 & y_3 & y_4 & y_5 & y_6 \end{bmatrix}^T \\
\frac{d\mathbf{y}}{dr} &= \mathbf{A}\cdot\mathbf{y} \\
\mathbf{A} &= \begin{pmatrix}
-2\lambda\sigma^{-1}r^{-1} & \sigma^{-1} & \lambda\sigma^{-1}Lr^{-1} & 0 & 0 & 0 \\
-4\rho_0 g r^{-1} + 4\gamma r^{-2} & 2(\lambda\sigma^{-1}-1)r^{-1} & (-2\gamma r^{-2} & Lr^{-1} & (l+1)r^{-1} & -\rho_0 \\
 & & +\rho_0 g r^{-1})L & & & \\
-r^{-1} & 0 & r^{-1} & \mu^{-1} & 0 & 0 \\
\rho_0 g r^{-1} - 2\gamma r^{-2} & -\lambda\sigma^{-1}r^{-1} & -2\mu r^{-2} & -3r^{-1} & -\rho_0 r^{-1} & 0 \\
 & & +(\gamma+\mu)Lr^{-2} & & & \\
4\pi G\rho_0 & 0 & 0 & 0 & -(l+1)r^{-1} & 1 \\
4\pi G\rho_0 & 0 & -4\pi G\rho_0 Lr^{-1} & 0 & 0 & (l-1)r^{-1}
\end{pmatrix},
\end{aligned} \tag{A22}$$

where

$$\begin{aligned}
\lambda &= \kappa(r) - \frac{2}{3}\mu(r,s) \\
\sigma &= \lambda(r,s) + 2\mu(r,s) \\
\gamma &= \lambda(r,s) + \mu(r,s) - \lambda^2(r,s)\sigma^{-1}.
\end{aligned} \tag{A23}$$

The system of coupled first-order differential equations A22 is to be integrated from Earth's interior to the surface subject to regularity at the center of the Earth and continuity of the six functions $y_1,\ldots,y_6$. However, if the surface of discontinuity is a solid-fluid interface,

© 2006 The Authors, *GJI*, **167,** 397–420
Journal compilation © 2006 RAS

then only y_1, y_2, y_4, y_5, and y_6 are continuous. In intended applications we assume a homogeneous fluid core of density ρ_c and the starting radius of integration is taken to be the core–mantle boundary. There are three independent solutions at $r = b$ given by

$$\mathbf{y}^I(b,s) = \begin{pmatrix} 0 \\ 0 \\ 1 \\ 0 \\ 0 \\ 0 \end{pmatrix}, \quad \mathbf{y}^{II}(b,s) = \begin{pmatrix} l \\ 0 \\ 1 \\ 0 \\ l\frac{4\pi\rho_c G}{3} b \\ l(l-1)\frac{8\pi\rho_c G}{3} \end{pmatrix}, \quad \mathbf{y}^{III}(b,s) = \begin{pmatrix} 1 \\ \rho_c g(b) \\ -\frac{1}{2} \\ 0 \\ 0 \\ -4\pi\rho_c G \end{pmatrix}. \tag{A24}$$

These are the the solutions for quasi-static deformation of a self-gravitating homogeneous solid sphere in the limit of vanishing shear modulus μ, and they were obtained by evaluating the solutions in eqs (27), (28), and (29) of Vermeersen *et al.* (1996) in the limit $s \to 0$. Note that one should split the $C(s)$ function in eq. (33) of Vermeersen *et al.* (1996) into two cases in order to prescribe their displacement-stress vectors correctly (Vermeersen & Sabadini 1997). The first solution corresponds to a discontinuity in horizontal displacement across the solid-fluid boundary. The boundary conditions given by eq. (48) of Wu & Peltier (1982) and eq. (20) of Saito (1974) are linear combinations of those given in eq. (A24) and therefore equivalent.

Vanishing traction and upward continuation of the gravity field at Earth's surface give the required boundary conditions at $r = a$:

$$\begin{aligned} y_2(r,a) &= a_1 y_2^{(I)}(r,a) + a_2 y_2^{(II)}(r,a) + a_3 y_2^{(III)}(r,a) = 0 \\ y_4(r,a) &= a_1 y_4^{(I)}(r,a) + a_4 y_2^{(II)}(r,a) + a_3 y_4^{(III)}(r,a) = 0 \\ y_6(r,a) &= a_1 y_6^{(I)}(r,a) + a_6 y_2^{(II)}(r,a) + a_3 y_6^{(III)}(r,a) = 0 \end{aligned}$$

for appropriate constants a_i. This requires the vanishing of the determinant

$$\begin{vmatrix} y_2^I(a,s) & y_2^{II}(a,s) & y_2^{III}(a,s) \\ y_4^I(a,s) & y_4^{II}(a,s) & y_4^{III}(a,s) \\ y_6^I(a,s) & y_6^{II}(a,s) & y_6^{III}(a,s) \end{vmatrix} = 0. \tag{A25}$$

The boundary conditions in eq. (A17) for toroidal motion or eq. (A25) for spheroidal motion are satisfied for a dispersion set of values $s = \{-s_j\}$. For a fixed l there are an infinite number of decay times if the Earth model contains a continuous spectrum of material relaxation times $\tau = \frac{\mu_0}{\eta_0}$. However, when the Earth model contains only a finite number of τ (e.g. in a case with a finite number of layers with different material properties), then the toroidal motion dispersion set for a fixed l contains a finite number of s_j, and similarly for the spheroidal motion dispersion in the absence of gravitation (Piersanti *et al.* 1995; Pollitz 1997) or for incompressible, gravitational Earth models with a finite number of layers (e.g. Piersanti *et al.* 1995; Wu & Ni 1996). However, relaxation of a compressible self-gravitating Earth model generally involves an infinite dispersion set (Vermeersen *et al.* 1996).

The transformed displacement field is inversely proportional to the determinant evaluated with eqs (A17) or (A25). Thus the dispersion sets contain the poles of the transformed displacement field. Assuming that these poles are simple poles, the time domain response is

$$\mathbf{u}(\mathbf{r},t) = \sum_j \mathbf{M} : \mathbf{E}_j(\mathbf{r}_s, \hat{\mathbf{r}})\epsilon_j^{-1} \frac{1 - \exp(-s_j t)}{s_j}, \tag{A26}$$

where $\mathbf{E}_j$ is an excitation function for the response to a moment tensor source (e.g. Appendix A of Pollitz 2003b) and

$$\begin{aligned} \epsilon_j &= L \int_0^a \left([r\partial_r y_1(r,-s_j) - y_1(r,-s_j)]^2 + (L-2)(y_1(r,-s_j))^2 \right) \\ &\quad \times \left. \frac{\partial \mu(r,s)}{\partial s} \right|_{s=-s_j} r^2\, dr, \end{aligned} \tag{A27}$$

for toroidal motion and

$$\begin{aligned} \epsilon_j &= \int_0^a \left(\left[\frac{1}{3} 2\partial_r y_1(r,-s_j) - F \right] + L r^{-2} [r\partial_r y_3(r,-s_j) - y_3(r,-s_j) + y_1(r,-s_j)]^2 \right. \\ &\quad \left. + r^{-2}(y_3(r,-s_j))^2 \left[2(L-1)L - L^2 \right] \right) \left. \frac{\partial \mu(r,s)}{\partial s} \right|_{s=-s_j} r^2\, dr \\ F &= r^{-1}[2y_1(r,-s_j) - L y_3(r,-s_j)], \end{aligned} \tag{A28}$$

for spheroidal motion.

APPENDIX B: STABLE INTEGRATION OF SPHEROIDAL MOTION SOLUTION

The Bulirsch–Stoer integration method (Press *et al.* 1996) is used to integrate both the toroidal and spheroidal systems of equations to high accuracy. For toroidal motion, it is straightforward to integrate eq. (A13) for the one independent solution y^I from the starting radius to Earth's surface and stably evaluate the determinant in eq. (A17) as a function of s. For spheroidal motion, however, one must integrate three solutions and evaluate the determinant in eq. (A25). In practice, the three solutions which are independent at the starting radius $r = b$ tend to be nearly linearly dependent at $r = a$ when the spherical harmonic degree is sufficiently large, even for wavelengths as long as ∼1000 km ($l = 40$). This results in an unstable evaluation of the determinant and large inaccuracies in the determination of y_i and possibly misidentification of poles s_j. Methods to address this problem include large l approximations of the solutions (e.g. Riva & Vermeersen 2002) and integration of systems of minors of the displacement-stress vector (Woodhouse 1988). We use a simple scheme that removes the linear dependence of the solutions by iterative adjustment of the solutions at the starting radius. The steps of this procedure are as follows:

(1) Define $\Lambda_0 = \mathbf{I}$ (the 3×3 identity matrix) and assign iteration number $i = 0$.
(2) Prescribe initial solutions at $r = b$

$$(\mathbf{y}^1 \quad \mathbf{y}^2 \quad \mathbf{y}^3) = (\mathbf{y}^I(b,s) \quad \mathbf{y}^{II}(b,s) \quad \mathbf{y}^{III}(b,s)) \cdot \Lambda_i, \tag{B1}$$

(3) Integrate the solutions $\{\mathbf{y}^{(k)} \,|k = 1, 2, 3\}$ to $r = a$. Exponentially increasing solutions are re-scaled where necessary to keep the $\mathbf{y}^{(k)}$ bounded and the scaling factors stored.
(4) Choose a solution $\mathbf{y}^{(k)}$ to use as a pivot to eliminate either $y_2(a,s)$ or $y_4(a,s)$ from the other two solutions. For this purpose we evaluate the second order minors

$$\begin{vmatrix} y_2^{(k')}(a,s) & y_2^{(k'')}(a,s) \\ y_4^{(k')}(a,s) & y_4^{(k'')}(a,s) \end{vmatrix}, \tag{B2}$$

divided by a measure of the size of the displacement-stress vectors, denoted by the product $|\mathbf{y}^{(k')}(a,s)| \times |\mathbf{y}^{(k'')}(a,s)|$, for pairs $(k', k'') = (1, 2), (1, 3), (2, 3)$. The pair with the smallest second order minor determines k, that is, the index not equal to k' or k''. The relative sizes of $y_2^{(k)}(a,s)$ and $y_4^{(k)}(a,s)$ determines whether y_2 or y_4 is eliminated from the other two solutions.
(5) For the sake of illustration, assume that $\mathbf{y}^{(1)}$ is chosen to eliminate $y_2^{(2)}(a,s)$ and $y_2^{(3)}(a,s)$. We define

$$\Lambda_1 = \begin{pmatrix} 1 & -\frac{y_2^{(2)}(a,s)}{y_2^{(1)}(a,s)} & -\frac{y_2^{(3)}(a,s)}{y_2^{(1)}(a,s)} \\ 0 & 1 & 0 \\ 0 & 0 & 1 \end{pmatrix}, \tag{B3}$$

(6) Repeat steps 2 and 3 for iteration $i = 1$. This yields a new set of solutions with theoretically

$$\begin{pmatrix} y_2^{(1)}(a,s) & y_2^{(2)}(a,s) & y_2^{(3)}(a,s) \\ y_4^{(1)}(a,s) & y_4^{(2)}(a,s) & y_4^{(3)}(a,s) \\ y_6^{(1)}(a,s) & y_6^{(2)}(a,s) & y_6^{(3)}(a,s) \end{pmatrix} = \begin{pmatrix} y_2^{(1)}(a,s) & 0 & 0 \\ y_4^{(1)}(a,s) & y_4^{(2)}(a,s) & y_4^{(3)}(a,s) \\ y_6^{(1)}(a,s) & y_6^{(2)}(a,s) & y_6^{(3)}(a,s) \end{pmatrix}, \tag{B4}$$

(7) Between those two displacement-stress vectors, which just had a component eliminated ($\mathbf{y}^{(2)}$ and $\mathbf{y}^{(3)}$ in this example), choose one of them to be a pivot to eliminate y_6 from the other two displacement-stress vectors. For this purpose we choose $\mathbf{y}^{(k)}$ with the largest $y_6^{(k)}(a,s)/|\mathbf{y}^{(k)}(a,s)|$. Assume that $\mathbf{y}^{(3)}$ is chosen.
(8) Define

$$\Lambda_2 = \Lambda_1 \cdot \begin{pmatrix} 1 & 0 & 0 \\ 0 & 1 & 0 \\ -\frac{y_6^{(1)}(a,s)}{y_6^{(3)}(a,s)} & -\frac{y_6^{(2)}(a,s)}{y_6^{(3)}(a,s)} & 1 \end{pmatrix}, \tag{B5}$$

(9) Repeat steps 2 and 3 for iteration $i = 2$. This yields a new solution with theoretically

$$\begin{pmatrix} y_2^{(1)}(a,s) & y_2^{(2)}(a,s) & y_2^{(3)}(a,s) \\ y_4^{(1)}(a,s) & y_4^{(2)}(a,s) & y_4^{(3)}(a,s) \\ y_6^{(1)}(a,s) & y_6^{(2)}(a,s) & y_6^{(3)}(a,s) \end{pmatrix} = \begin{pmatrix} y_2^{(1)}(a,s) & 0 & 0 \\ y_4^{(1)}(a,s) & y_4^{(2)}(a,s) & y_4^{(3)}(a,s) \\ 0 & 0 & y_6^{(3)}(a,s) \end{pmatrix}, \tag{B6}$$

(10) Evaluate the determinant

$$\begin{vmatrix} y_2^{(1)}(a,s) & y_2^{(2)}(a,s) & y_2^{(3)}(a,s) \\ y_4^{(1)}(a,s) & y_4^{(2)}(a,s) & y_4^{(3)}(a,s) \\ y_6^{(1)}(a,s) & y_6^{(2)}(a,s) & y_6^{(3)}(a,s) \end{vmatrix}. \tag{B7}$$

© 2006 The Authors, *GJI*, **167,** 397–420
Journal compilation © 2006 RAS

This method is found to be very effective in removing the linear dependence of the three starting solutions. The determinant evaluated in step 10 is extremely close to that evaluated in iteration 0 when the trial value of s is far from a pole. However, as s approaches a pole, the determinant evaluated in step 10 is typically several orders of magnitude smaller than that evaluated in iteration 0. The former is a smooth function of s, whereas numerical round-off error produces a highly discontinuous value of the latter.

The negative real $s-$ axis is divided into a large number of intervals, and successive bisection is used to find where the determinant vanishes and estimate the pole locations $s = -s_j$. Once the three starting solutions are integrated upward in iteration 2 at such a pole, it is straightforward to reconstruct the displacement-stress vector components $y_1, \ldots, y_6$ as a function of radius.

© 2006 The Authors, *GJI*, **167,** 397–420
Journal compilation © 2006 RAS